Science Advances

AAAS

Supplementary Materials for

Reconciling atmospheric CO₂, weathering, and calcite compensation depth across the Cenozoic

Nemanja Komar* and Richard E. Zeebe

*Corresponding author. Email: komar@hawaii.edu

This PDF file includes:

1 Model description

The overall modeling framework in this study combines and expands two geochemical models: LOSCAR (Long-term Ocean-atmosphere Sediment CArbon cycle Reservoir) and GEOCARB III. The details of the two models (in their original form) are thoroughly documented in (*15*) and (*17*), thus we refrain from providing a detailed description of all of the models' components and designs here. However, the modifications applied to the original versions of each model as well as the connection between the models will be discussed here.

LOSCAR is a carbon cycle box model that can operate on both short-term (centuries) and long-term (millions of years) time scales, efficiently computing the partitioning of carbon between various model components (ocean, atmosphere and sediments) but unlike GEOCARB, it does not include the geologic carbon cycle, so the two complement each other (*5*). In LOSCAR, the world oceans are represented with three (four in the palaeo version) major ocean reservoirs (Atlantic, Indian, Pacific, and Tethys in the palaeo set-up). Each of the basins is subdivided into three different boxes (shallow, intermediate, and deep) and there is one generic box representing the high latitude ocean. Thus, there is a total of ten (thirteen in the paleo version) ocean boxes

plus an additional box representing the atmosphere. The model keeps track of various biogeo-chemical tracers (including total carbon-TC, total alkalinity-TA, stable carbon isotopes-δ^{13}C, and others) in the different boxes. Using the model predicted concentrations of TC and TA in the individual ocean boxes, and supplying them to the chemistry routines described by (*58*), parameters such as [CO_2], [CO_3^{2-}], pH and calcite saturation state are calculated. The chemical routines allow for variations in the [Ca^{2+}] and [Mg^{2+}] of seawater as well as for the temperature changes. This is critical because varying Mg/Ca ratio and temperature affect the thermodynamics (e.g. equilibrium constants and solubility products of chemical reactions), and therefore can alter the predicted ocean carbonate chemistry and atmospheric pCO_2 (*5*). As both ocean temperature and Mg/Ca ratio have varied considerably over the simulated period (Fig. S1) the model had to be adjusted accordingly (see Section 1.1).

1.1 Model modifications, data acquisition, and model coupling

1.1.1 GEOCARB module

The input data used in the original GEOCARB III model is relatively coarse, with a resolution that exceeds 10 million years. As the primary purpose of the original GEOCARB model was describing the behavior of carbon cycle across the entire Phanerozoic ($\sim$ 570 Ma), this type of accuracy is justified. Nevertheless, any events that occurred on time scales shorter than 10 Ma could not be properly modeled and such a model would be impractical for the purposes of this study (*5*).

One of the main model inputs is the δ^{13}C of bulk sediments (*59*), which is used to calculate burial rates of carbonate carbon and organic carbon. Using the δ^{13}C data of bulk sediments that have a resolution greater than 1 million years (1 Myr is the time-step of GEOCARB) is therefore crucial. Fortunately, since the model inception, numerous carbon isotope data sets with a higher resolution and updated age models have become available (*1, 3, 49, 60, 61*). GEOCARB was thus accordingly modified to utilize the new data sets in order to capture the processes of the

long-term carbon cycle during the Cenozoic more accurately. This modified version is referred to as the GEOCARB module (*5*).

The $\delta^{13}C$ data implemented by the original GEOCARB III model were replaced by two data sets of much higher temporal resolution, placed on a current timescale. For the time period between 58 and 48 Ma we use $\delta^{13}C$ records at Deep Sea Drilling Projects Sites 527 and 577 (*4, 61*). The remainder of the $\delta^{13}C$ record (48 Ma to present) comes from the bulk sediment $\delta^{13}C$ data presented in (*49*). To prevent rapid and abnormal model fluctuations produced by abrupt changes in $\delta^{13}C$ data caused by the hyperthermal events and other short-lived events during the Cenozoic, the data was smoothed using a local linear kernel estimator with a constant bandwidth of one million years (*62, 63*). This approach is justified because the focus of this study is on long-term carbon cycle behavior rather than short-term variations.

1.1.2 LOSCAR-P

Both the original LOSCAR model and GEOCARB lack a long-term P cycle, thus neglecting the influence of the marine biota on long-term C cycling. On long time scales, dissolved phosphorus is a biolimiting nutrient in the ocean (*64*) and therefore the primary regulator of organic matter production (*65*). As such, the C and P cycles are linked because the availability of dissolved P affects the rate of organic carbon burial (*66, 67*). Another link is through atmospheric pCO_2 and oxygen saturation (see below). High pCO_2 and therefore accelerated weathering fluxes could in theory also intensify the supply of nutrients to the ocean (*68*), potentially leading to higher biological carbon production and export, and ultimately to higher carbon burial. This close connection between the P and C cycles is the rationale for expanding the original LOSCAR model to also include a long-term P cycle. The expanded version of LOSCAR will be referred to as LOSCAR-P. The LOSCAR-P model has previously been used to explain the rapid Earth-system recovery following a carbon cycle perturbation during the PETM (*16*), where the building blocks of LOSCAR-P and therefore alterations performed on the original LOSCAR model are thoroughly discussed. The same LOSCAR-P model is utilized here with several important

adjustments highlighted below.

Unlike all of the previous modeling exercises performed by LOSCAR, which simulate ocean-atmosphere chemistry over a few hundred thousand years, here simulations span tens of millions of years (*5*). Due to the time scale over which the simulations are performed it is crucial to account for changes of parameters which exert great influence on marine carbonate chemistry across the Cenozoic. The original LOSCAR model has two different configurations and thus two sets of boundary conditions; one for modern ocean and the other representing the Late Paleocene conditions. In order to fill the gap, the boundary condition parameters for other time epochs had to be reconstructed from paleo-proxies or by linear interpolation. These parameters include variable oceanic Mg^{2+} and Ca^{2+} concentrations (variable Mg/Ca ratio), and temperature. Other parameters that are considered and that are of great importance are changing bathymetry, thermohaline circulation, vertical mixing rates, the rain ratio between organic and inorganic carbon being exported from the surface ocean (r_{rain}), and the ratio of shelf to open ocean production (fsh).

Magnesium and Calcium concentration in sea water varied throughout Earth's history. Paleo-proxies for Mg and Ca concentration in the world oceans show a monotonously increasing and decreasing trends over the Cenozoic, respectively (*69*). The changing Mg and Ca concentrations have profound implications for dissolution of $CaCO_3$ in sea water as these ions affect the ocean carbon system. Because of their importance in determining the saturation state of sea water, all simulations incorporate varying $[Mg^{2+}]$ and $[Ca^{2+}]$ based on the data compiled by (*69*) (Fig. S1).

Over geologic time the area, depth profiles, and volumes of ocean basins vary noticeably. The original LOSCAR model already implements realistic volumes of ocean boxes for modern ocean (*70*) and Late Paleocene ocean (*71*). The basin volumes and the depth profiles for other epochs are missing and were reconstructed by linear interpolation between the two data sets. Changes in areas of individual ocean across Eocene and Oligocene were generated by linearly interpolating between Late Paleocene (*71*) and and Middle Miocene (*72*) bathymetries. The evo-

lution of ocean areas between the Middle Eocene and present was reconstructed by interpolating the Middle Miocene (*72*) and modern (*70*) bathymetry. For more details on bathymetry, see (*73*) and (*74*) who collected the bathymetry data and performed the above mentioned interpolations.

The next set of LOSCAR parameters described below are not well constrained in deep geologic times and their modern and/or the Late Paleocene values were obtained by model tuning (except for modern thermohaline circulation). These parameters include the conveyor (thermohaline) transport, vertical ocean mixing, and r_{rain}. The modern thermohaline circulation in LOSCAR is 20 Sv (1 Sv = $10^6 m^3 s^{-1}$) (*75*) and the Late Paleocene is set to 25 Sv (*15*). The thermohaline transport (and other parameters outlined above) across the rest of the Cenozoic was attained by linear interpolation between the two given values (modern vs. Late Paleocene). In the modern ocean, the Thermohaline circulation is powered by sinking cold waters in the North Atlantic (North Atlantic Deep Water formation, NADW for short). This circulation scheme in the Late Paleocene was different, with cold waters forming in the Southern Ocean (SO formation). We implement a gradual shift from primarily NADW formation to SO dominated circulation between time t = 0 to t = 23 Ma. The remainder of the parameter values (vertical ocean mixing, r_{rain}, relative size of shelf versus deep ocean) were kept the same for Late Paleocene and modern ocean (Table S2) as in the original LOSCAR (*5*).

The P cycle in this version of LOSCAR-P is slightly different from the orginal one described in (*16*). The modern (pre-industrial) P fluxes and their boundary conditions now follow the range of values provided in (*76*) (see Table S1). Because the LOSCAR-P model does not differentiate between shallow ocean and deep ocean organic P and C burial, the initial P fluxes used in LOSCAR represent the sum of shallow and deep fluxes presented in (*76*). Unlike in the previous LOSCAR-P version (*16*), where the pre-PETM phosphorus fluxes were rather arbitrarily chosen and considered to be in steady-state, here P and org C burial fluxes at any point in the past depend on the modern values. The modern LOSCAR-P model conditions assume that the P cycle is in steady-state (inputs equal outputs; see Table S1). The P and C burial fluxes are redox-dependent, and in this model version, the fluxes depend on the mean deep ocean oxygen

concentration:

$$F_{bp} = f_{bp} \times F_{Pexp} \times \left(0.25 + 0.75 \frac{[O_2]}{[O_2]_0} \right) \times \frac{F_{crain}}{F_{crain_0}}, \tag{1}$$

where f_{bp} is the fraction of the P export flux that is buried in the sediments, initially set to ∼0.5% to satisfy steady state (see Table S1). This flux is also dependent on water column oxygenation (76, 77) and organic carbon rain reaching the sediments (78). $[O_2]_0$ is the mean deep water oxygen concentration at time t = 0 (0.25 $\frac{mol}{m^3}$). Burial of organic P is reduced by up to 75% under full anoxia, while the burial of organic carbon increases (76, 77).

The F_{bp} and F_{bg} fluxes are coupled through the organic matter C to P burial ratio, which is significantly larger than the Redfield value (76, 77, and references therein). This ratio, just like F_{bp} also depends on the redox-state of the water column (77):

$$\frac{F_{bg}}{F_{bp}} = \frac{\left(\frac{C}{P}\right)_{oxic} \times \left(\frac{C}{P}\right)_{anox}}{\frac{[O_2]}{[O_2]_0} \times \left(\frac{C}{P}\right)_{anox} + \left(1 - \frac{[O_2]}{[O_2]_0}\right) \times \left(\frac{C}{P}\right)_{oxic}}, \tag{2}$$

where $\left(\frac{C}{P}\right)_{oxic}$ = 317 (calculated to satisfy steady-state, see Table S1) and $\left(\frac{C}{P}\right)_{anoxic}$ = 1100 (76), represent end-member values for organic matter buried under completely oxic and fully anoxic deep water conditions, respectively.

The P flux associated with ferric iron oxides is linearly correlated to changes in oxygen concentration of the deep water (77):

$$F_{FeP} = F_{FeP}^0 \times \frac{[O_2]}{[O_2]_0}, \tag{3}$$

where F_{FeP}^0 is F_{FeP} at time t = 0 (pre-industrial steady-state rate).

Precipitation of authigenic CaP is formulated as follows (77):

$$F_{CaP} = f_{CaP} \times POP_{remin} \times \left(0.1 + 0.9 \frac{[O_2]}{[O_2]_0} \right) \tag{4}$$

where f_{CaP} is a fraction of reactive P that is produced by decomposition of organic matter and is converted into CaP. Its value is $\sim$0.01 and is set to satisfy the pre-industrial steady-state condition (see Table S1). POP_{remin} is remineralization flux of P, which is equal to the difference between export and burial. Thus:

$$POP_{remin} = F_{Pexp} \times (1 - f_{bp}).\qquad(5)$$

The phosphorus weathering flux (F_{pw}) is a function of silicate and carbonate weathering rates with slight modifications:

$$F_{pw} = F_{pw}^0 \times \frac{F_{Si}}{F_{Si}^0},\qquad(6)$$

where F_{pw}^0, and F_{Si}^0 are riverine input of dissolved phosphorus, and silicate weathering at time t = 0 (modern steady-state), respectively.

Phosphorus and organic C burial differs from that of carbonate as there is no explicit diagenetic sediment model associated with the burial of P and organic C. In other words, once buried P and organic C are permanently stored and cannot be reintroduced back to the water column. Also, LOSCAR-P does not differentiate between burial of C and P in the deep sea vs. margin. However, it is important to note that the burial numbers that the model produces represent the total global burial rates (shelf + deep combined), because organic C and P burial processes are essentially modeled as one box. Nevertheless, additional modeling experiments show that the locale of organic C and P burial has numerically insignificant influence on the results. That is, the model produces the exact same output regardless of whether organic C and P are fully buried in shallow or deep ocean. Furthermore, the results produced by LOSCAR-P are in line with carbon, phosphorus and oxygen cycle models that include both shelf and open ocean sedimentary burial (77). The model of (77) shows that organic C burial is enhanced in both ocean regions (shallow and deep) during oxygen depletion. On the other hand, P burial rates exhibit different behavior between margins and deep ocean. In the model of (77), which has a separate

representation of the shelf and deep ocean burial, low oxygen conditions promote lower P burial rates in the deep sea (the same behavior as in LOSCAR-P2), while on the shelf P burial rates increase (*77*). However, the total net burial rate (shelf + deep) of P during the low oxygen conditions is diminished compared to the steady-state oxygen conditions, which matches predictions made by our model. Additionally, on long-time scales ($> \sim$10 kyr), P is well mixed throughout ocean, hence the differences between shelf versus deep ocean are less critical.

1.1.3 Coupling

Numerically, the GEOCARB module has been implemented as a function that is called from within LOSCAR (Fig. S2). At time t = 0 (modern, pre-industrial ocean) all GEOCARB and LOSCAR fluxes match. Once LOSCAR is initiated, it uses the GEOCARB module to obtain carbon fluxes (except organic C burial) for any particular point in the past in one million-year step intervals (the time step of GEOCARB). LOSCAR then uses its own boundary conditions for a particular point in the past (e.g. 58 Ma; thus vertical mixing, temperature, $[Ca^{2+}]$ and $[Mg^{2+}]$ and other parameters all change, see Table S2) and is run for 1 million years to calculate a new value for organic carbon burial (which depends on the feedback between carbon, oxygen and phosphorus as well as on temperature). The newly calculated organic carbon burial flux is then supplied to the GEOCARB module, where a Newton-Raphson method is invoked in order to calculate a new $\delta^{13}C$ value necessary to balance all the fluxes at the given time step. The calculated $\delta^{13}C$ value is then compared with the actual $\delta^{13}C$ input data of GEOCARB to see how far the LOSCAR-P $\delta^{13}C$ (and thus LOSCAR-P organic C burial rate) deviates from observations (and thus from organic C burial rate predicted by GEOCARB). Because both LOSCAR-P and GEOCARB use the same pCO_2-weathering feedback, once the organic carbon burial is the same in both models, so will be carbonate (F_{wc}) and silicate weathering (F_{Si}) fluxes (*5*):

$$F_{wc} = fbb(\mathbf{CO_2}) \times f_{LA} \times f_D \times f_E \times F_{wc}^0, \tag{7}$$

$$F_{Si} = fb(\text{CO}_2) \times f_R \times f_E \times f_D^{0.65} \times F_{Si}^0, \tag{8}$$

where fbb and fb are functions that account for the effects of $p\text{CO}_2$ on carbonate and silicate weathering rates (see (79)), respectively. F_{wc}^0 and F_{Si}^0 are modern carbonate and silicate weathering rates, respectively (see Table S1 for modern values). f's are dimensionless parameters accounting for various biogeochemical process through geologic time (Fig. S3 and Ref. (79)).

2 Martin curve and temperature dependency

The temperature change in the model is prescribed based on the observed $\delta^{18}\text{O}$ temperature proxy data (Fig. S4) following the relationship (47):

$$T_t = 16.9 - 4.0 \times (\delta^{18}\text{O}_t - \delta^{18}\text{O}_{sw}), \tag{9}$$

where $\delta^{18}\text{O}_t$ is the observed data and $\delta^{18}\text{O}_{sw}$ is the $\delta^{18}\text{O}$ of the seawater at a given time in the past:

0 to 10 Ma = -0.2

10 to 34 Ma = -1.0

34 to 58 Ma = -1.2

As explained in the main text, the particulate organic carbon attenuation factor in Martin curve appears to be dependent on temperature (40, 42, 80). As such, the amount of carbon reaching the sea floor is determined by the median ocean temperatures (Fig. S5). Thus, as the global Earth temperature changes throughout the Earth past so does the amount of carbon reaching the sea floor.

3 Sensitivity studies and model-data discrepancies

Without the assumed effect of temperature on remineralization rates, the model is unable to reproduce carbon isotope excursion trends as well as the change in atmospheric pCO_2 for time periods older than $\sim$25 Ma (Fig. S8a-b; control run). The discrepancies between the model results and data are most obvious during the Paleocene and Eocene, when the Earth was much warmer than today and when atmospheric CO_2 concentrations were several times that of the modern (preindustrial) atmosphere (*6, 81*). The main culprit for the erroneous model behavior are the high organic carbon burial rates that arise as a result of the positive feedback loop between carbon, oxygen, and phosphorus (C-O-P feedback) (*5*). For example, the control run exhibits peak organic carbon burial rates at 52 Ma, when deep ocean oxygen concentration is at its lowest due to high temperatures. This time period coincides with the highest dissolved P concentrations and low total P burial (Fig. S9). Low oxygen concentrations favor enhanced organic carbon preservation while diminishing organic phosphorus burial due to increased remineralization. Higher organic P respiration in turn fuels the surface ocean with recycled organic P and enhances the primary production and results in even larger organic carbon export (*5*).

The problem with the modeling approach described above is that it assumes that any excess in delivery of dissolved P to the surface ocean (whether through increased continental supply or via deep ocean P recycling) and thus rising surface ocean [PO_4] will not only increase export production from the surface ocean but also result in an increased amount of carbon being deposited in the deep ocean (strong carbon "pump"). Because of tight coupling between surface ocean [PO_4], primary productivity, and export production, the above modeling approach will necessarily lead to high organic carbon burial rates (and a positive ^{13}C excursion) during periods of increased warming (*5*). In order to reconcile the observed δ^{13}C and CO_2 it was necessary to assume a temperature dependent organic matter respiration. When invoked, this mechanism results in high atmospheric CO_2 during warmer time periods, while at the same time results in more negative δ^{13}C values (e.g. compare simulations 0 and 1, Fig. S8 and S10, respectively),

which is consistent with the observations (Fig. S18).

Nevertheless, while the general trends in temperature dependent scenario are consistent when the temperature dependent organic C and P burial is invoked, absolute changes in magnitude are not. For example, the observed mean bulk carbonate δ^{13}C decrease during the LPEE is about 2.0‰, whereas the model captures approximately only half of the observed negative excursion ($\sim$1.00‰). It has been shown that the δ^{13}C trend between 58 and $\sim$52 Ma is difficult to explain from the conventional carbon cycle standpoint. The combined global climate change indicators during this time interval imply an existence of a dynamic organic carbon capacitor that can accumulate and discharge large quantities of isotopically depleted ^{13}C into the ocean-atmosphere system (*4*). Only when an organic capacitor (e.g. methane hydrate capacitor) is included (Fig. S18; (*4*)), the model produces a data consistent negative δ^{13}C excursion during the LPEE.

The model-data δ^{13}C discrepancies during the rest of the Cenozoic (e.g. $\sim$13 - 20 Ma) could arise from at least two possible reasons. First, the δ^{13}C value of the riverine input is kept constant throughout the run. Changes in type of the material being preferentially weathered, and/or changes in proportion of the amount of organic carbon being weathered relative to carbonate carbon, at different climates and across different time intervals, could very well cause variations in the carbon isotopic value of the riverine flux. Second, it could be possible that the absolute organic carbon burial rates predicted by the model underestimate/overestimate the actual organic burial rates during the periods of the model-data divergence (*5*).

3.1 Sea level and CaCO$_3$ proliferation

To reconcile the CCD trends it was necessary to assume a sea level dependent shelf to deep CaCO$_3$ fractionation factor (fsh), as well as an additional fsh amplification prior to the Eocene-Oligocene boundary ($\sim$34 Ma). The relationship between the sea level height and shelf-deep CaCO$_3$ fractionation in the model is justified as the carbonate accumulation on the shelves is correlated with the sea level variations across the Cenozoic (*30,31*). The fsh curve (Fig. S7a) was

normalized to the sea level curve such that the fsh value for Paleocene would be approximately equal to the default fsh value of the original LOSCAR model for this time period. This required normalizing the sea level curve between 1 (modern fsh) and 7 (maximum sea level at 50 Ma). Note, however, that the fsh value is just a factor, which proportionates the relative amount of carbon rain between the shelf and deep ocean. The total shelf to deep ratio and the total $CaCO_3$ burial does not scale linearly with fsh (Fig. S7b).

In order to reproduce the shallow Paleogene CCD, it was also necessary to scale fsh up by a factor of three in the model during this time period (Fig. S7a). The resulting calculated mean shelf $CaCO_3$ burial rate predicted by the model in our reference scenario prior to the Eocene-Oligocene (EO) boundary (34 to 58 Ma; $\sim 20 \times 10^{12}$ mol/yr) is ~ 3 higher than for the post EO boundary period ($\sim 6 \times 10^{12}$ mol/yr). This is consistent with the relative trends of the observed carbonate mass accumulation rate during the same time interval, which shows that the shelf carbonate accumulation prior to the EO boundary was about two to three times higher than post the EO boundary (*30*). The higher mass carbonate accumulation rate on the shelf during the high Paleogene sea level stand was not only due to the longitudinal expansion of carbonate platforms, which was a function of the larger shelf area, but also due to the latitudinal expansion of carbonate platforms (*30, 31*). During the periods of low sea level stand, such as today, carbonate accumulation is confined to a narrow latitudinal band (between 30 degrees north and south. However, the data points that the carbonate accumulation was expanded to 45 degrees north and south during the early Cenozoic (*30*). The latitudinal carbonate expansion during the warm periods, such as during the Late Paleocene and Early Eocene, is likely due to a lower $CaCO_3$ saturation gradient between the poles and the equator "*in response to more equable global climates*" (*30*).

In addition to the expansion of shallow carbonate platforms, which reached their peak during the warm period of Paleocene-Eocene (*30*), there is also evidence that the calcareous species richness (diversification) in the Cenozoic is well correlated with climate trends as well (*33*). The Cenozoic diversity maximum coincides with the Paleocene/Eocene epoch, the period of

extreme warmth. And during the cool period of Late Eocene and into the Oligocene, the species richness exhibits a decline, tracking the climate cooling (*33*). The Cenozoic diversity maximum (Paleocene-Eocene) was two to three times higher compared to the species richness after the Eocene-Oligocene boundary (*33*).

The observed latitudinal carbonate platform expansion combined with the observed species richness increase during the Late Paleocene/Early Eocene and the relative magnitude of the increase are on par with the shelf carbonate burial evolution reproduced in our model in our preferred scenario using the fsh forcing described above. To summarize, the amplified fsh forcing used during Paleogene simulates the proliferation, migration, and latitudinal expansion of shelf ocean calcifiers during the epoch, which in turn reproduces the observed CCD more closely. The effect of fsh on the CCD evolution is best illustrated in the sensitivity studies (Fig. S18).

Table S 1: Modern steady state fluxes of phosphorus and organic carbon for the control model run. All units are in mol yr^{-1} except for isotopic values.

Symbol	Fluxes	Value	Notes
F_{Cexp}	Total carbon export	$\sim 424 \times 10^{12}$	
F_{Pexp}	Biological fixation of reactive P	3.260×12^{10}	$\frac{F_{Cexp}}{130}$[1]
F_{bg}	Org. C burial	5.000×10^{12}	e.g. Ref. (79)
f_{bg}	fraction of F_{Cexp} buried	1.2%	Based on Martin curve
F_{bp}	Org. P burial	1.575×10^{10}	Ref. (76)
f_{bp}	fraction of F_{Pexp} buried	0.5%	$f_{bp} = \frac{F_{bp}}{F_{Pexp}}$
F_{CaP}	CaP burial	3.150×10^{10}	Ref. (76)
f_{CaP}	fraction of reactive P converted into CaP	0.0097	$f_{CaP} = \frac{F_{bp}}{Pexp - F_{bp}}$
F_{FeP}	FeP burial	1.575×10^{10}	Ref. (76)
F_{wg}	Kerogen oxidation	5.000×10^{12}	to satisfy steady-state
F_{wc}	Carbonate weathering	12.00×10^{12}	Ref. (79)
F_{bc}	Inorganic C burial	17.00×10^{12}	Ref. (79)
F_{Si}	Silicate weathering	5.000×10^{12}	$F_{bc} - F_{wc}$; Ref. (79)
F_{pw}	Phosphate weathering flux	6.300×10^{10}	$F_{bp} + F_{CaP} + F_{FeP}$
$\left(\frac{C}{P}\right)_{oxic}$	C to P ratio at fully oxic conditions	317	$130 \times \frac{f_{bg}}{f_{bp}}$
$\delta^{13}C_{vc}$	Carbon isotope value of volcanic flux	-4.00 ‰	constant
$\delta^{13}C_{wc}$	Carbon isotope value of riverine flux	$+2.00$ ‰	constant

---

[1] Redfield Ratio

[2] Linearly interpolated from 0 Sv at t = 24 Ma (when Tethys first appears) to 2 Sv at 58 Ma.

[3] Linearly interpolated from 100% to 0 from 0 Ma to 23 Ma, before which NADW contribution is 0%.

[4] Linearly interpolated from 0 to 100% from 0 Ma to 23 Ma, after which SO contribution remains at 100%.

[5] Surface, Intermediate, Deep, and high latitude boxes, respectively.

[6] The number does not represent the total deposition ratio. The fsh parameter adjusts the relative amount of shelf to open ocean production.

[7] see Table S4 for fsh values used for each of the simulations

Table S 2: Physical and biogeochemical model boundary condition.

Parameters	Symbol	Modern	Late Paleocene	Other intervals	Unit
Thermohaline Transport	TH	20	25	interpolated	Sv
Tethys Transport	TH_T	–	2	interpolated[2]	Sv
NADW	–	100	0	interpolated[3]	%
SO	–	0	100	interpolated[4]	%
Temperature	T	20,10,2,2 [5]	Eq.(9)	Eq.(9)	${}^oC$
Shelf/deep parameter	fsh[6]	1	see Fig. S7	depends on simulation [7]	–
Rain ratio	r_{rain}	6.1	6.7	interpolated	–

Table S 3: Parameter values and equations.

Description	Value/Equation
Bottom depth of the Intermediate Ocean	$D_m = 1000$ m
Normalized hypsometry (interm. and deep)	$A^*_m = p_{m1}z^3 + p_{m2}z^2 + p_{m3}z + p_{m4}$
	$A^*_d = p_{d1}z^3 + p_{d2}z^2 + p_{d3}z + p_{d4}$
Hypsometry polynom. coeff. interm. $(z>-D_m)$	$p_{m1} = 0.307; p_{m2} = 0.624; p_{m3} = 0.430; p_{m4} = 0.991;$
Hypsometry polynom. coeff. deep $(z<-D_m)$	$p_{d1} = 0.02; p_{d2} = 0.103; p_{d3} = 0.219; p_{d4} = 1.025;$
Burial efficiency	$\beta = \alpha \times (b_1 exp[-b_3 \times -z \times 1000^{-1}] + b_2)$
Coupling of the organic C to organic P (α)	$\alpha = \dfrac{\left(\frac{C}{P}\right)_{oxic} \times \left(\frac{C}{P}\right)_{anox}}{\frac{[O_2]}{[O_2]_0} \times \left(\frac{C}{P}\right)_{anox} + \left(1 - \frac{[O_2]}{[O_2]_0}\right) \times \left(\frac{C}{P}\right)_{oxic}} \times F_{bp} * c$
Burial efficiency polynomial coefficients	$b_1 = 0.411; b_2 = 0.153; b_3 = 1.0;$
Burial efficiency scaling coefficient	c = 0.4
Organic carbon burial	see eqs. (3 and S2)
Organic carbon rain	see eq. (4)
Organic carbon remineralization	see eqs. (5 & 6)

Table S 4: Summary of the model simulations and forcing parameters. The null simulation does not have any additional assumption. Every successive simulation builds on the previous but an additional assumption is made

Simulation #	Assumptions	Figures
0.	No additional assumptions Temperature independent respiration Constant shelf to deep $CaCO_3$ fractionation	Figs. S8-9
1.	Temperature dependent Martin curve Constant shelf to deep $CaCO_3$ fractionation	Figs. S10-11
2.	Temperature dependent Martin curve Shelf to deep $CaCO_3$ fractionation a function of sea level	Figs. S12-13
3.	Temperature dependent Martin curve Shelf to deep $CaCO_3$ fractionation a function of sea level calcareous organism proliferation	Figs. S14-15
4.	Temperature dependent Martin curve Shelf to deep $CaCO_3$ fractionation a function of sea level Calcareous organism proliferation Organic carbon capacitor during the LPEE	Figs. S16-17
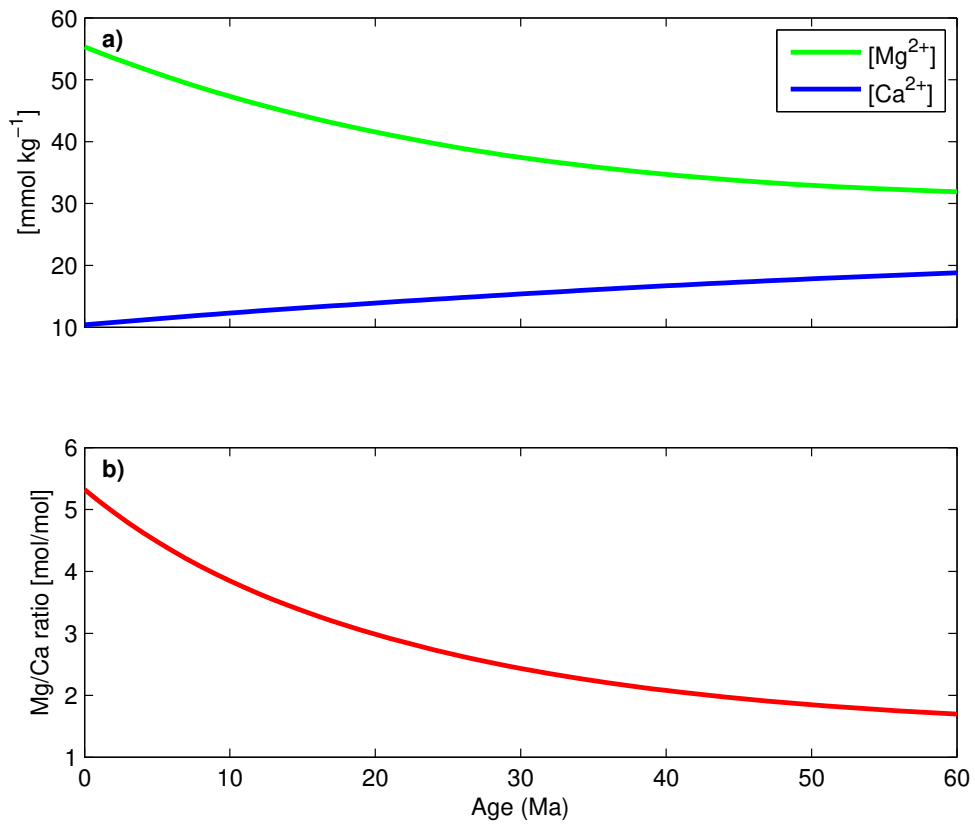
Figure S 1: Cenozoic Mg and Ca concentrations. Cenozoic Mg and Ca concentrations. a) Magnesium concentration. The lines are calculated by cubic interpolation of the Cenozoic Ca and Mg concentrations data compiled by (*69*) b) The Mg/Ca ratio calculated from the data in panel "a".

(0) t = 0 Ma (modern):
   LOSCAR-P fluxes = GEOCARB fluxes

(1) t = t + 1 Ma,
   Call GEOCARB module

LOSCAR-P

GEOCARB
module

(3) Inputs   (5) F_{bg}

(4) LOSCAR
   outputs

(2) GEOCARB
   outputs

F_{bg}, CCD, $\delta^{13}C_{surf}$,
$\delta^{13}C_{deep}$, pH, DIC, TA, etc.

F_{wc}, F_{mc}, F_{wg}, F_{mg}, F_{Si}

(6) GEOCARB
   outputs
   (with new F_{bg})

(7) Back to step #1

LOSCAR-P fluxes =
GEOCARB fluxes
(due to the same
weathering-pCO$_2$ feedback
in both models)
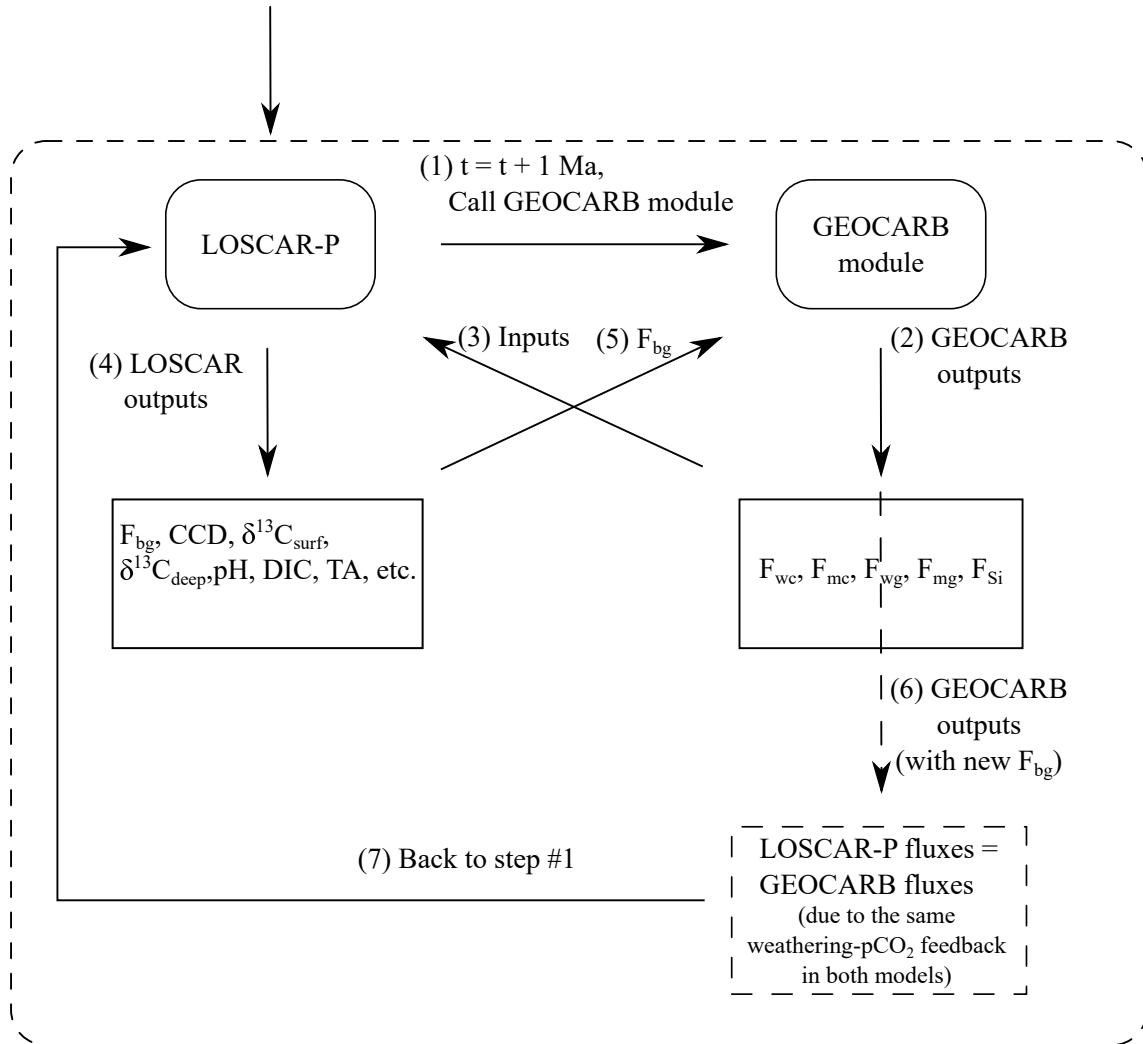
Figure S 2: LOSCAR-P − GEOCARB coupling schema.
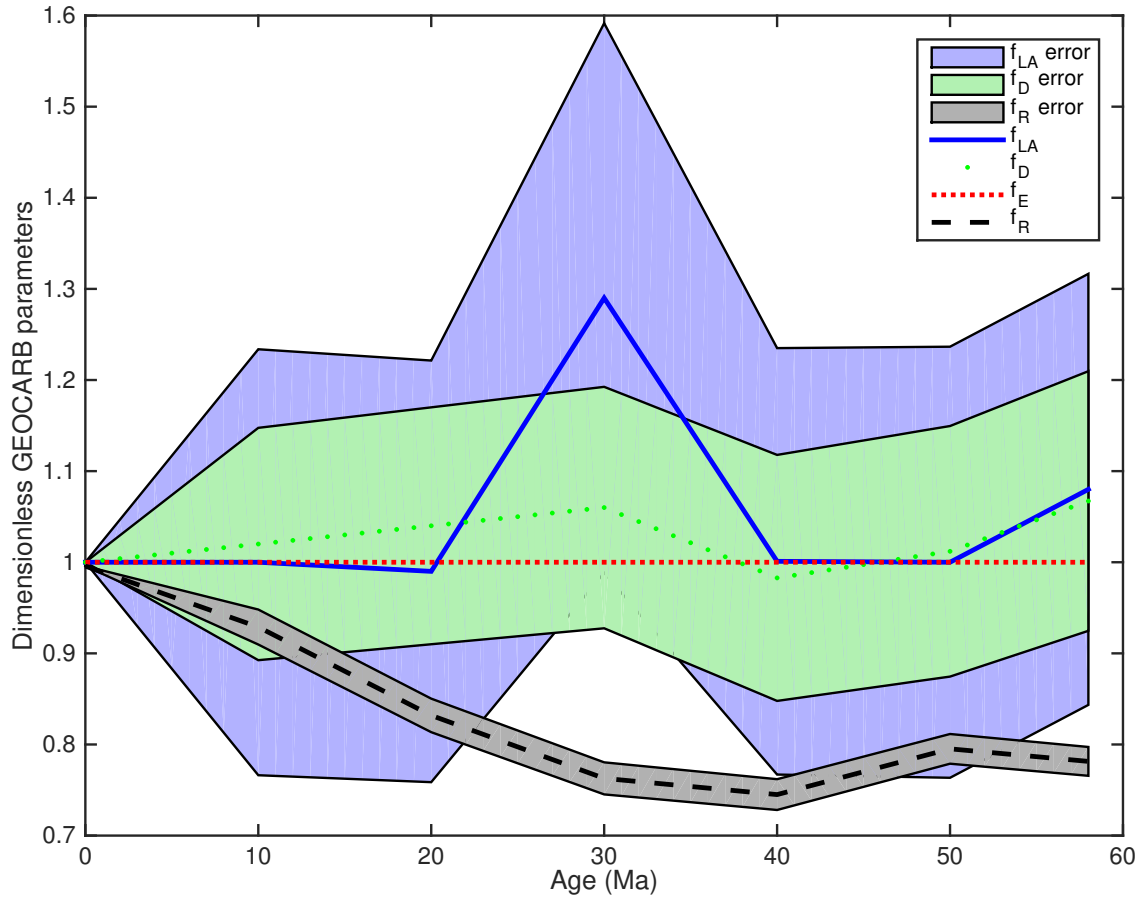
Figure S 3: Dimensionless GEOCARB parameters that account for various biological and geo-
logical factors across the Cenozoic (resolution = 10 Myr). All parameters are expressed relative
to modern. f_{LA}: describes the changes in the land area of carbonates available for weathering,
f_D: describes changes in river runoff due to variations in palaeogeography, f_E: soil biological
activity of land plants and their influence on weathering rates, f_R: represents the mean global
relief relative to present. The shaded area represents the parameters uncertainty envelope (*57*),
used for the model error envelope calculation (Fig 2.)
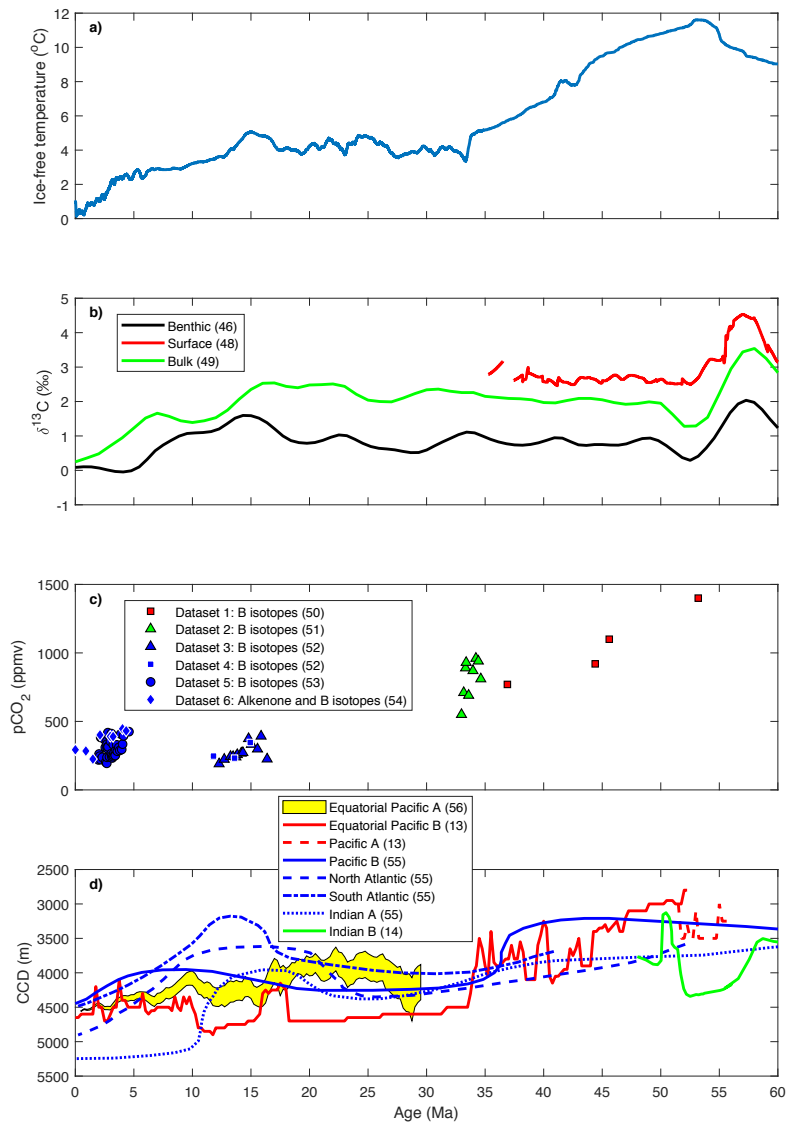
Figure S 4: Compilation of Cenozoic temperature, δ^{13}C, pCO$_2$, and CCD history for different ocean basins. (a) Global deep ocean temperature (*46*), (b) δ^{13}C compilation at different depths (Benthic: (*46*), Surface: (*48*), Bulk: (*49*), (c) atmospheric CO$_2$ reconstruction: Dataset 1 (*50*), Dataset 2 (*51*), Dataset 3 (*52*), Dataset 4 (*52*), Dataset 5 (*53*), Dataset 6 (*54*), and expressed in parts per million by volume (ppmv). "+" symbol stands for "et al." (d) Pacific, Atlantic and Indian Ocean CCD expressed in meters (m) below sea level. Equatorial Pacific A compiled from (*55*), Equatorial Pacific B and Pacific A from (*13*), Pacific B, North Atlantic, South Athlantic and Indian A from (*56*), and Indian B from (*14*). Hyperhermals are excluded from the original Indian ocean CCD data (*14*) (green line).
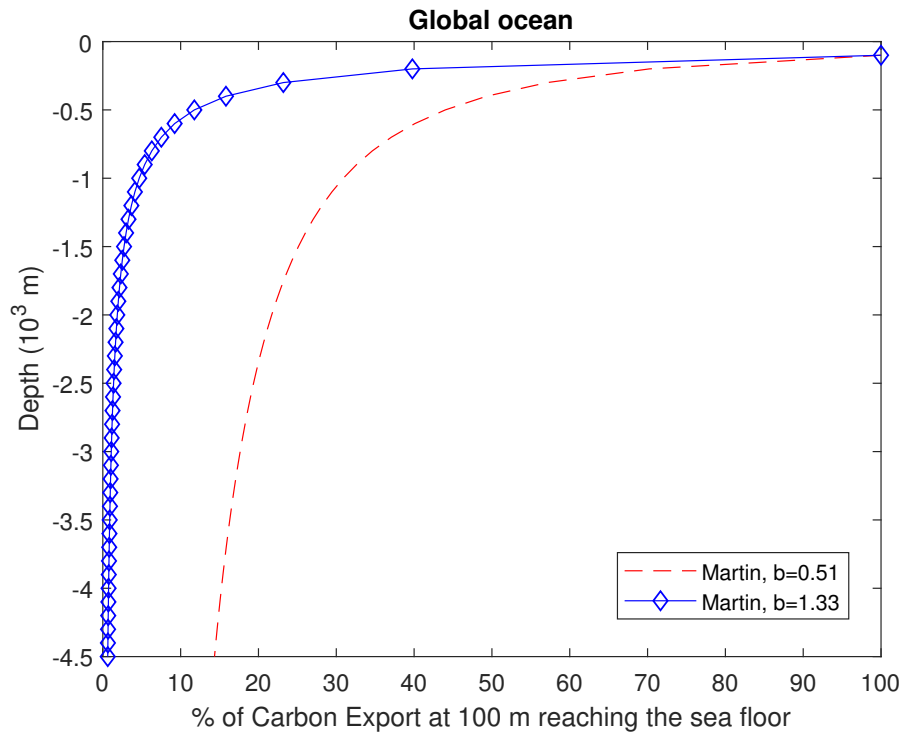
Figure S 5: Martin curve for two end members exponents for modern ocean (*42*). The X axis is expressed as the percentage of organic carbon exported at 100 meters depth reaching the sea floor at different depths. The blue (open diamonds) line represents colder water, where median temperature of the upper 500 m T = ~3.3^{o}C, and for warmer waters (red line, dashed line), T = ~17°C.
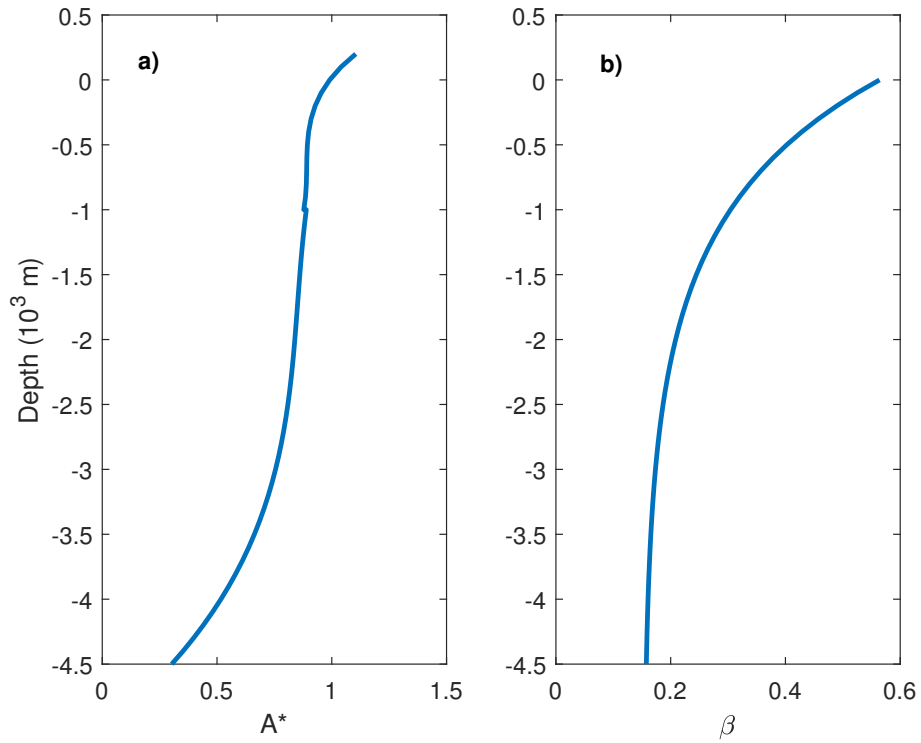
Figure S 6: The normalized hypsometric curve and organic carbon efficiency as a function of depth. a) "Normalized hypsographic curve $(A^*(z) = A(z) (A_0)^{-1})$, where $A(z)$ is ocean area at depth z and A_0 is ocean surface area at present." (*43*) The line represents cubic polynomial fitted to modified global mean from ETOPO5 data set (see Table S3). b) Initial (t = 0) burial efficiency (β) of organic carbon dependent on depth (see Table S3).
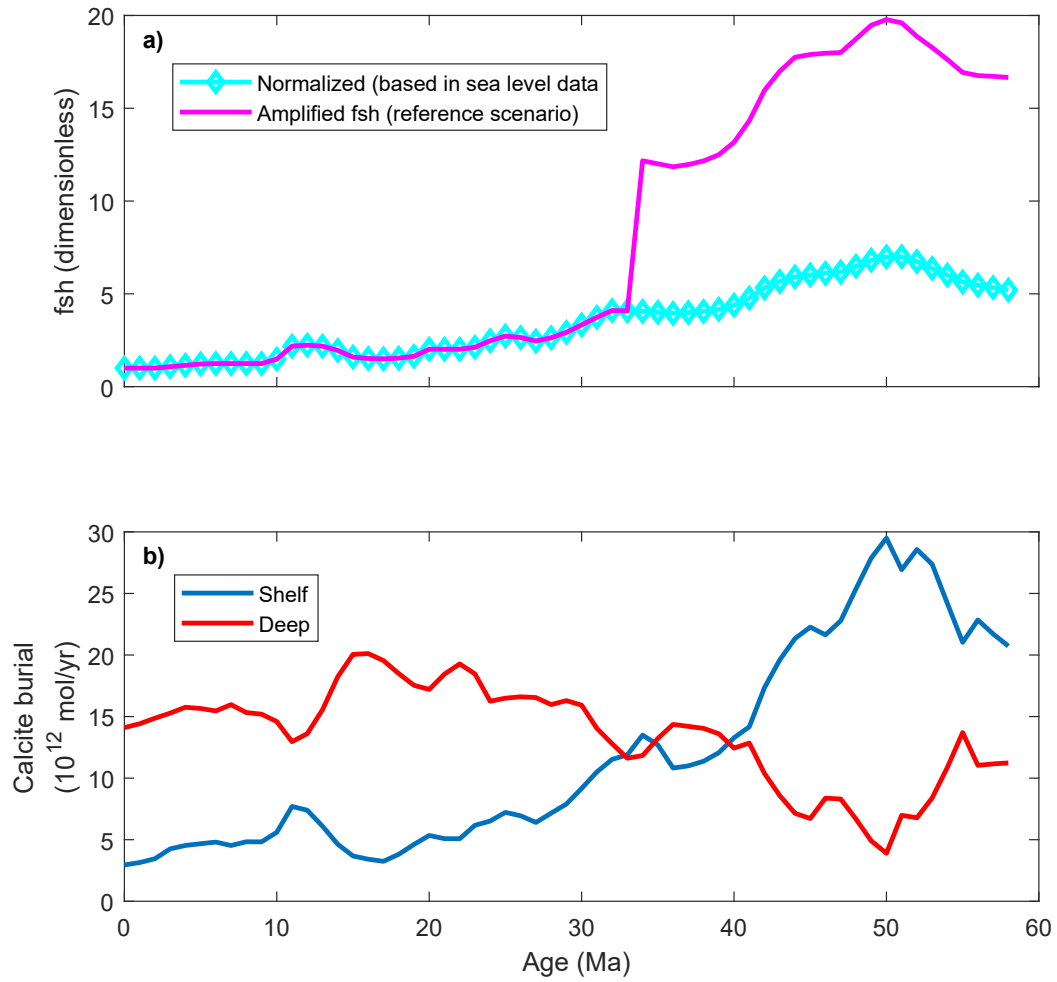
Figure S 7: Shelf to deep CaCO$_3$ fractionation forcing used in the model. a) fsh is normalized to the sea level curve (*82*) with the additional amplification prior to the Eocene-Oligocene boundary, simulating CaCO$_3$ organism proliferation and latitudinal expansion. b) predicted CaCO$_3$ burial rate evolution during the Cenozoic for the reference scenario.
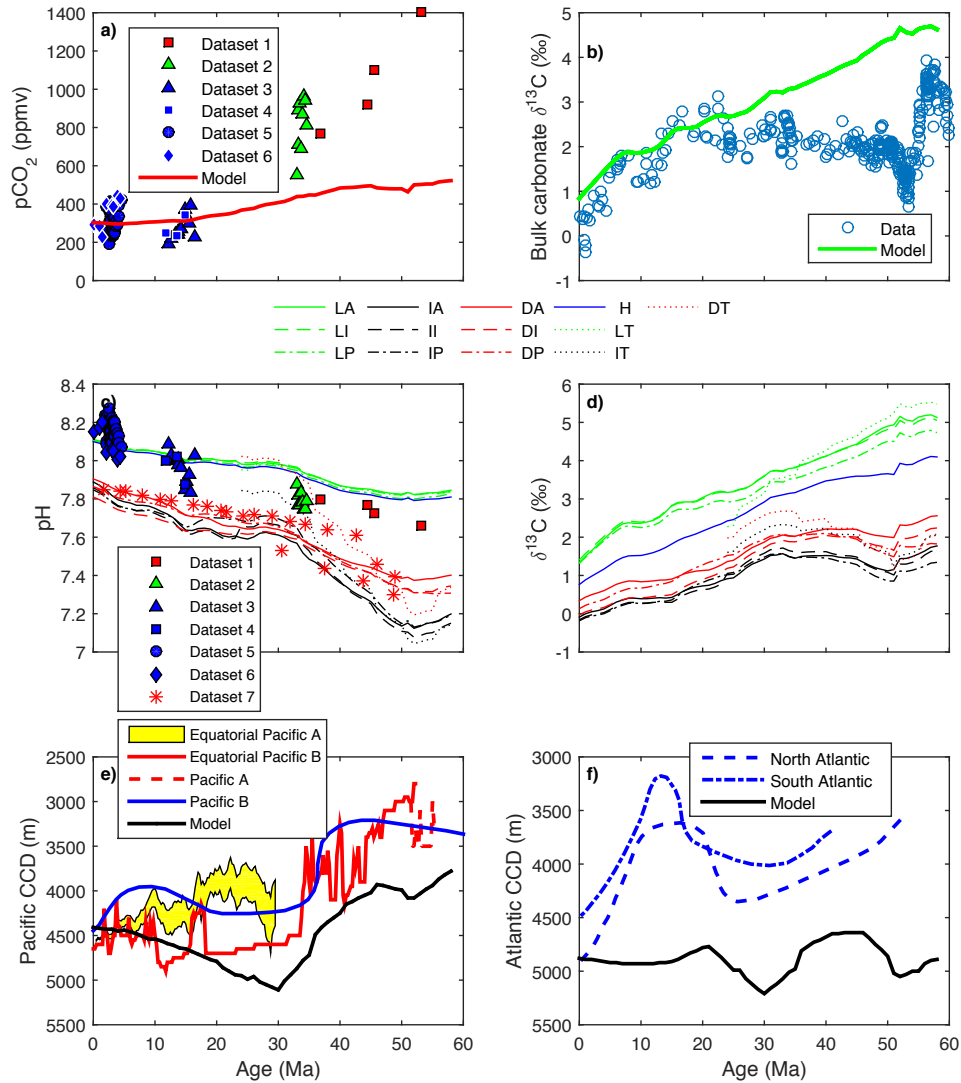
Figure S 8: Data − model comparison of various model results for the control run (Simulation 0. Table S4). a) Atmospheric pCO$_2$. The continuous red line is the model result and the symbols represent the data (See Fig. S4 for symbols description and references). b) Bulk carbonate δ^{13}C data (open circles) (*49*) versus model predicted bulk carbonate δ^{13}C (green line). c) Model predicted pH versus pH reconstructed from paleo-proxies, Dataset 1 through Dataset 7 compiled from (*50–54, 83*), respectively. d) Evolution of δ^{13}C in all ocean boxes. e) Model predicted evolution of the Pacific CCD against the Pacific CCD data (*13*). f) Model predicted evolution of the Atlantic CCD against the Atlantic CCD data (*56*).
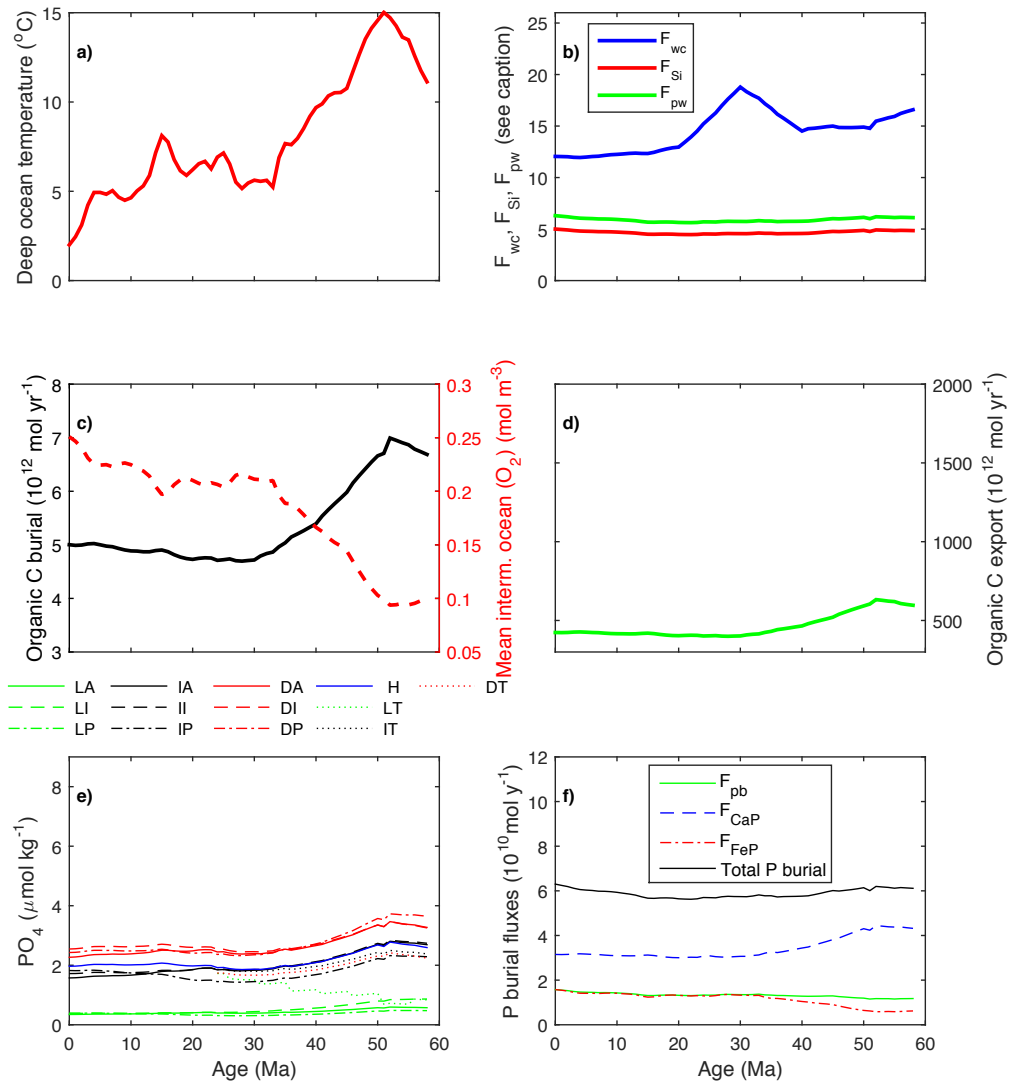
Figure S 9: Fluxes and additional model tracers for the control run (Simulation 0. Table S4).
a) The Cenozoic deep ocean temperature reconstruction (*46*), which is prescribed in the model
b) LOSCAR-P evolution of carbonate, silicate and phosphorus weathering fluxes. c) LOSCAR-P predicted organic carbon burial rate (solid line) and mean deep ocean oxygen concentration (dashed line). d) Total global organic carbon export form the surface ocean. e) Phosphate concentration in all LOSCAR-P boxes. "L" stands for low latitude surface ocean, "I" is intermediate, "D" is deep ocean, and "H" is the high latitude ocean. A,I,P and T correspond to Atlantic, Indian, Pacific, and Tethys ocean, respectively. f) Phosphorus burial fluxes.
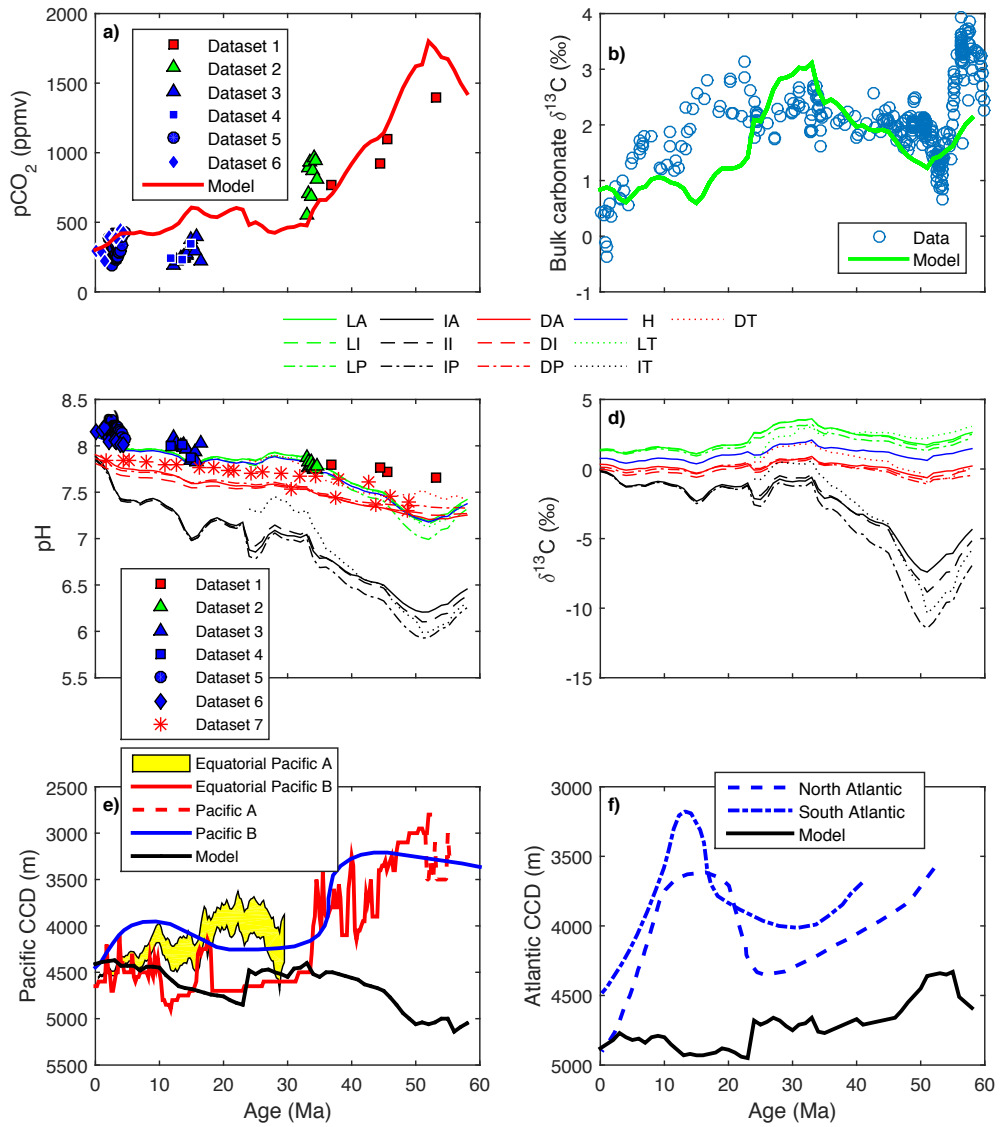
Figure S 10: Data − model comparison of various model results for Simulation 1. For individual panel description, refer to Fig. S8. See Table S4 for further explanation.
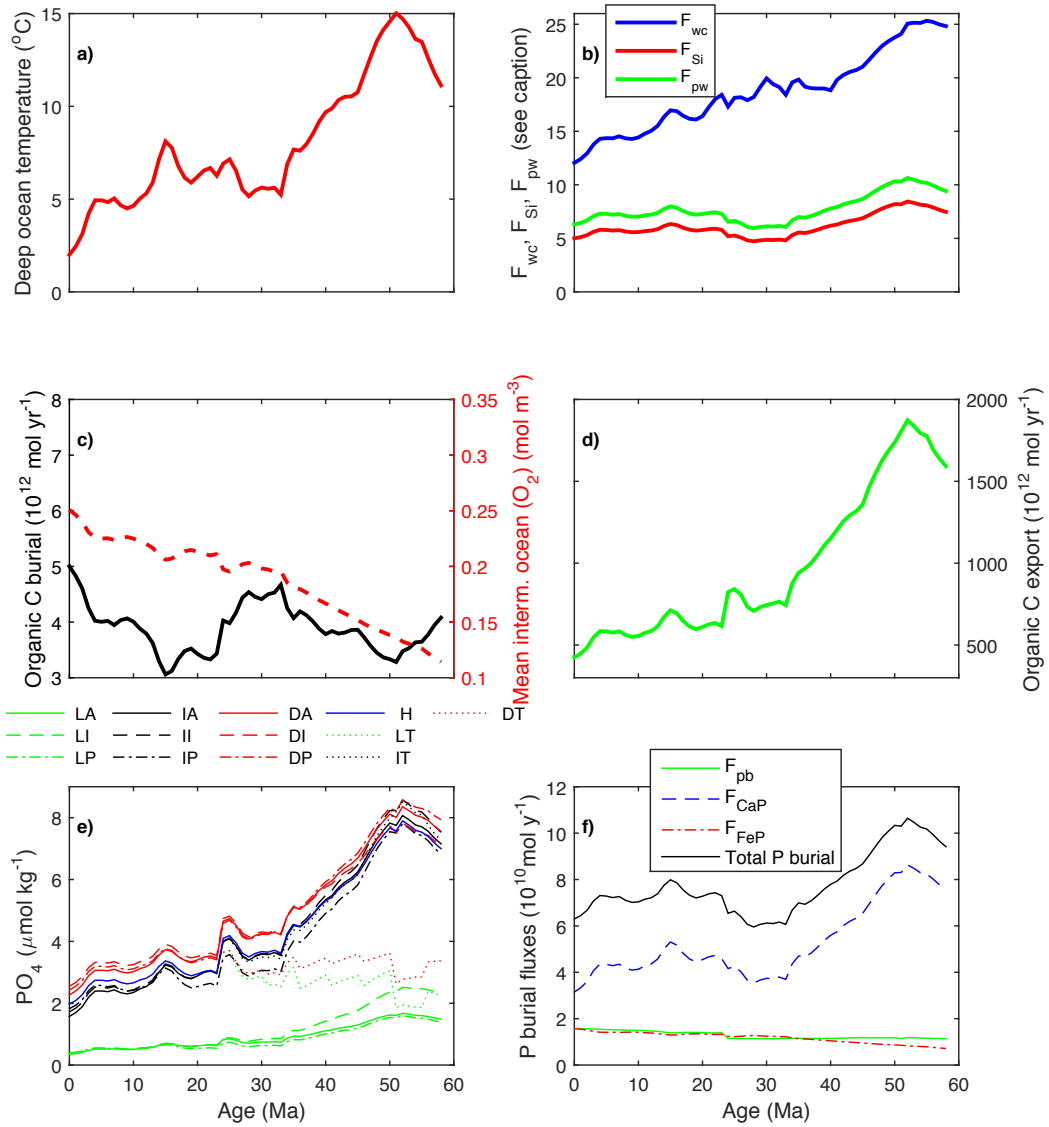
Figure S 11: Fluxes and additional model tracers for the control run (Simulation 1. Table S4).
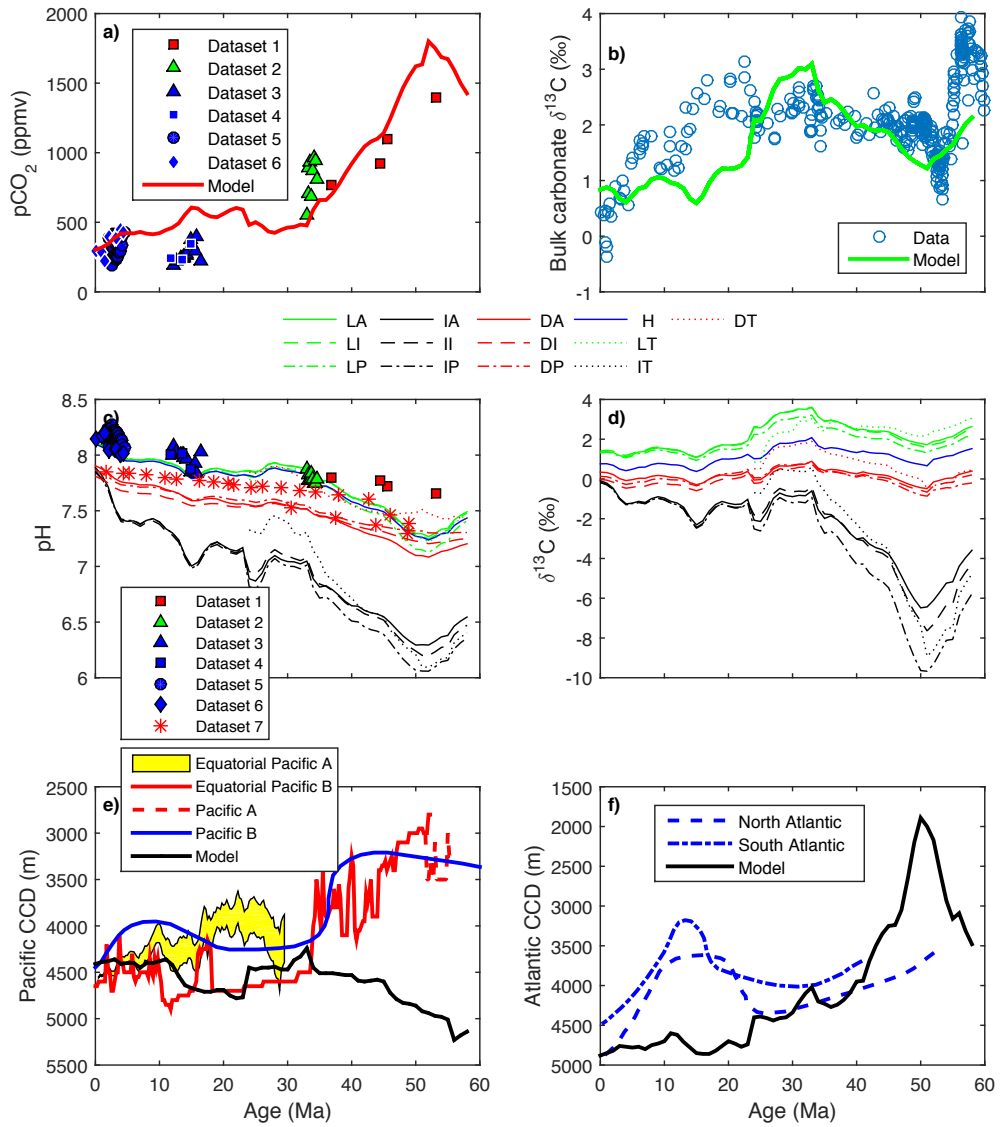For individual panel description, refer to Fig. S9. See Table S4 for further explanation.

Figure S 12: Data − model comparison of various model results for Simulation 2. For individual panel description, refer to Figure 8. See Table S4 for further explanation.
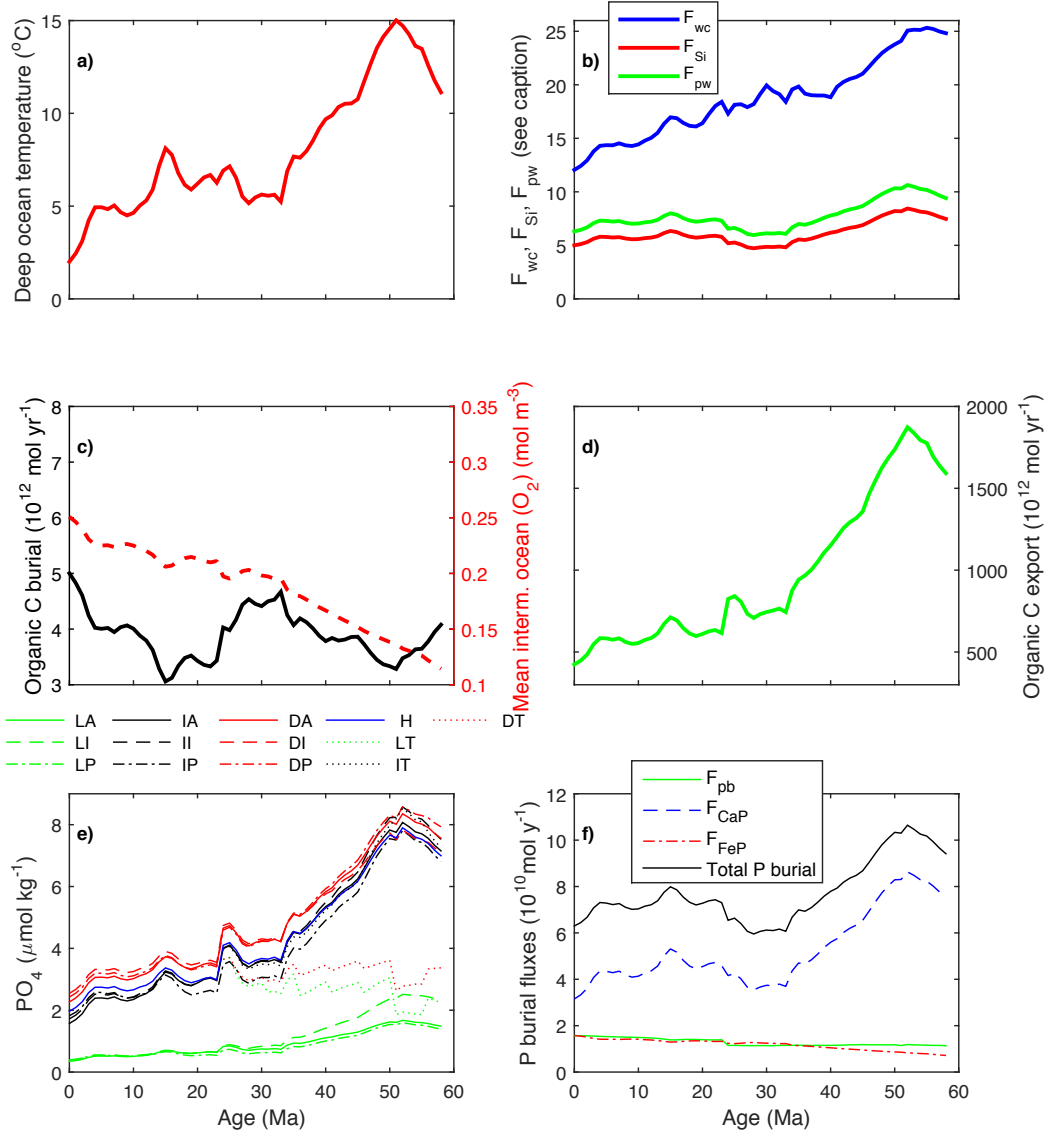
Figure S 13: Fluxes and additional model tracers for the control run (Simulation 2. Table S4). For individual panel description, refer to Fig. S9. See Table S4 for further explanation.
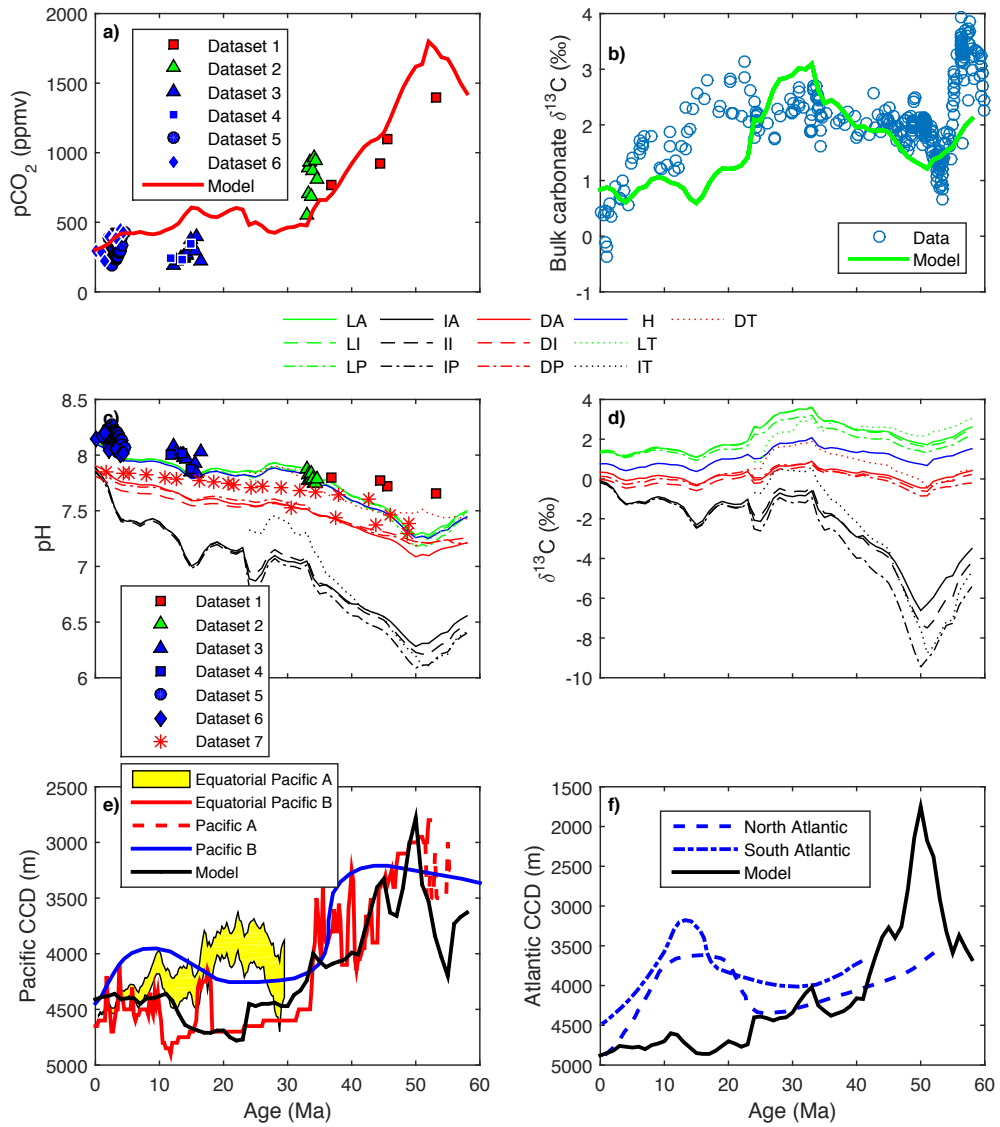
Figure S 14: Data — model comparison of various model results for Simulation 3. For individual panel description, refer to Fig. S8. See Table S4 for further explanation.
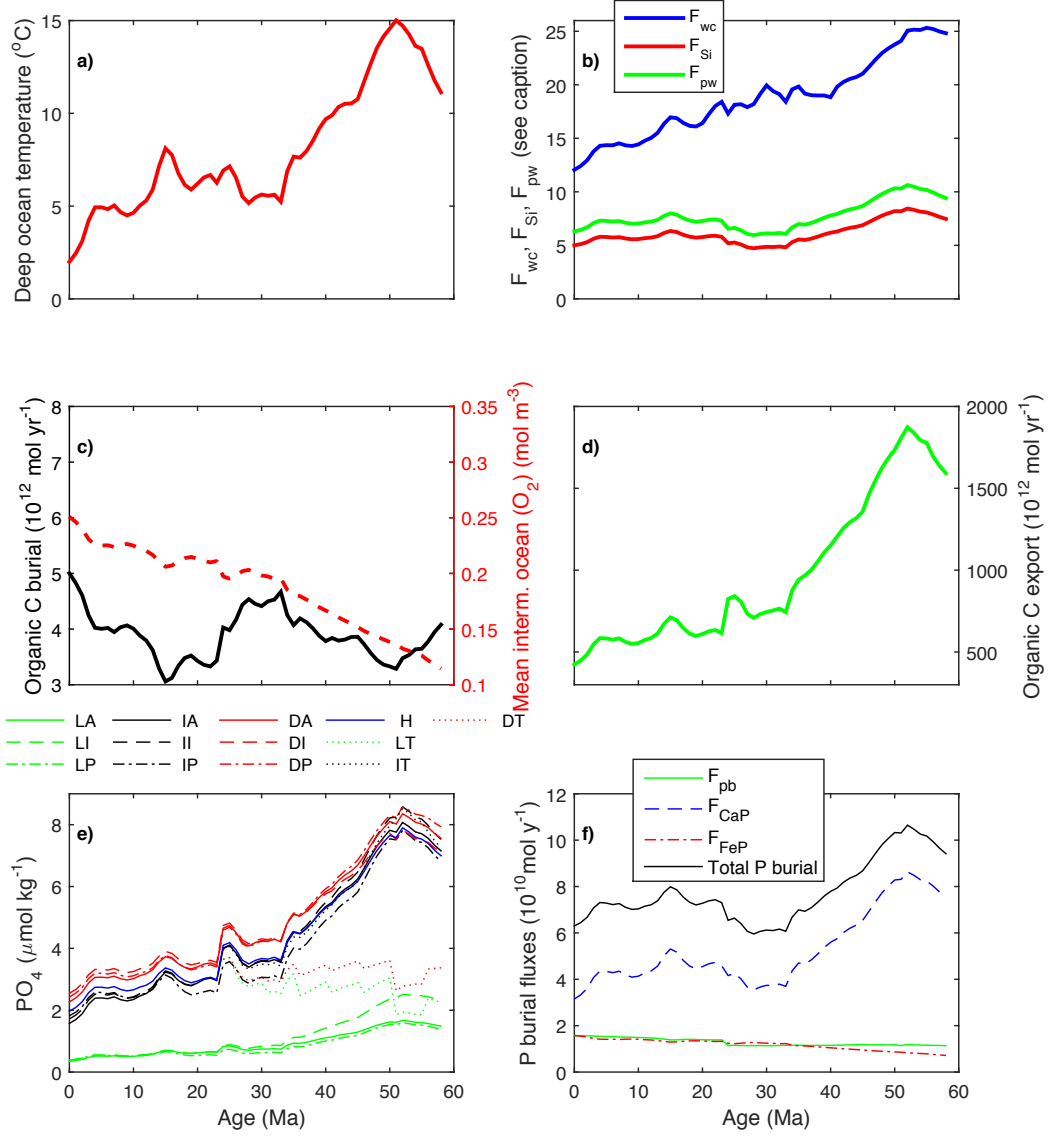
Figure S 15: Fluxes and additional model tracers for the control run (Simulation 3. Table S4). For individual panel description, refer to Fig. S9. See Table S4 for further explanation.
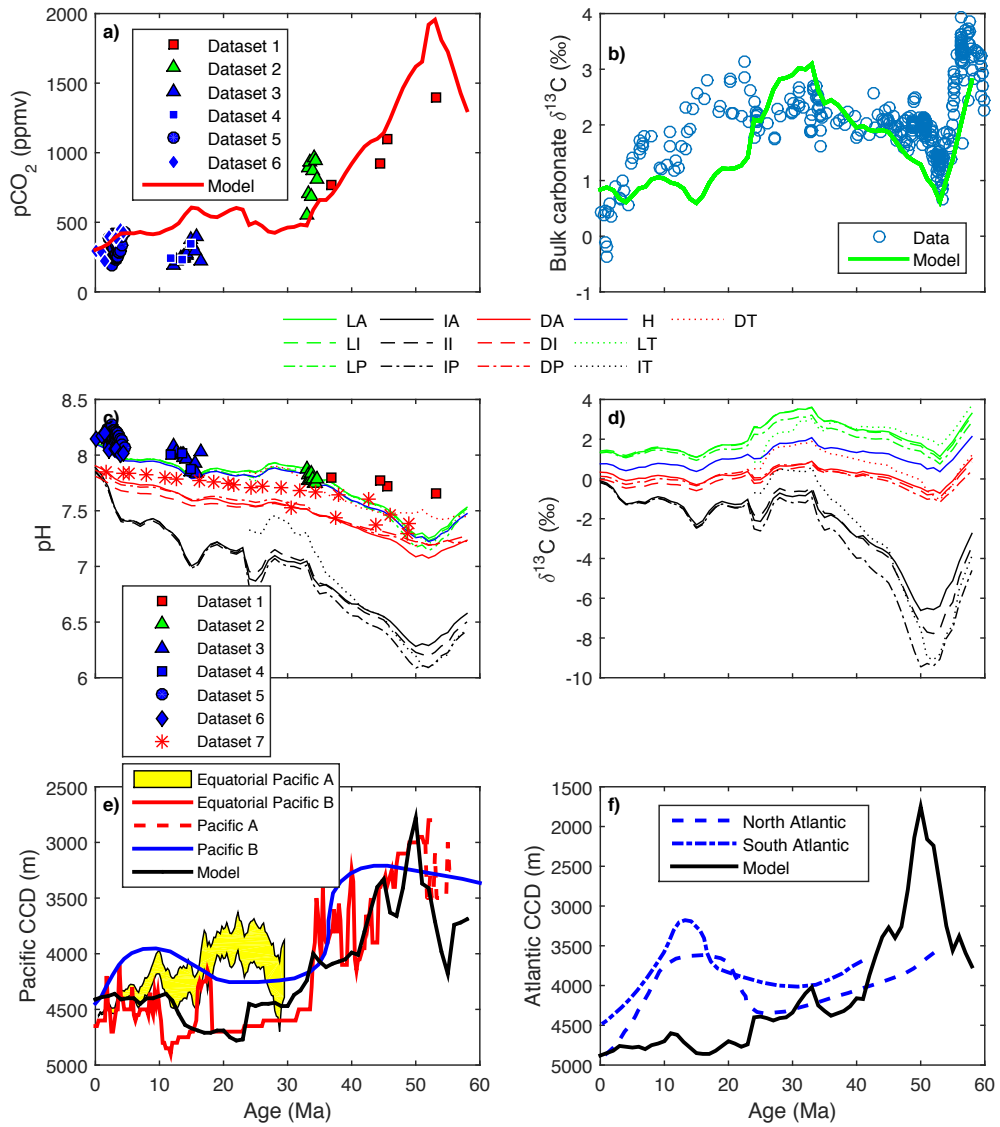
Figure S 16: Data − model comparison of various model results for Simulation 4. For individual panel description, refer to Fig. S8. See Table S4 for further explanation.
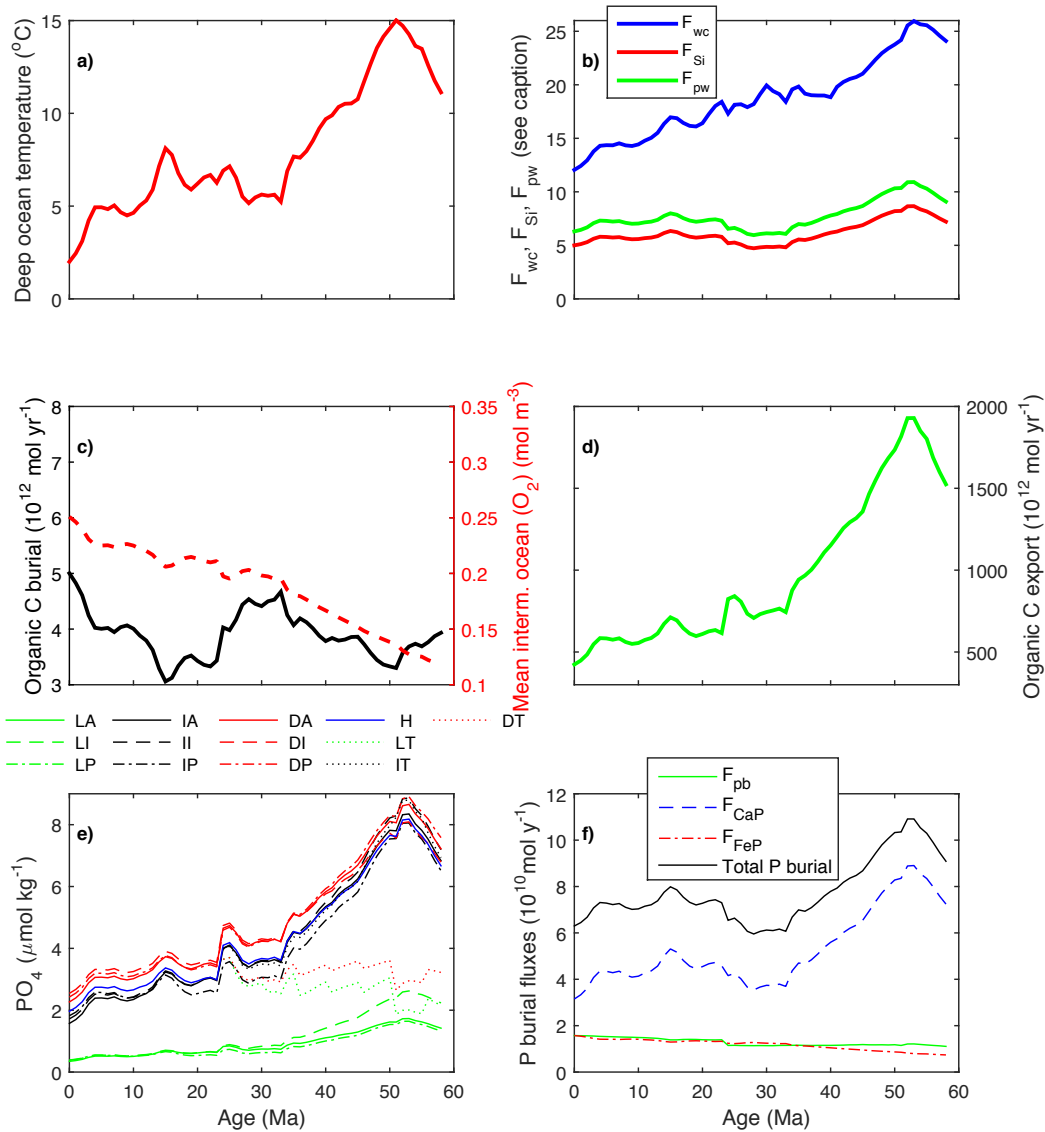
Figure S 17: Fluxes and additional model tracers for the control run (Simulation 4. Table S4). For individual panel description, refer to Fig. S9. See Table S4 for further explanation.
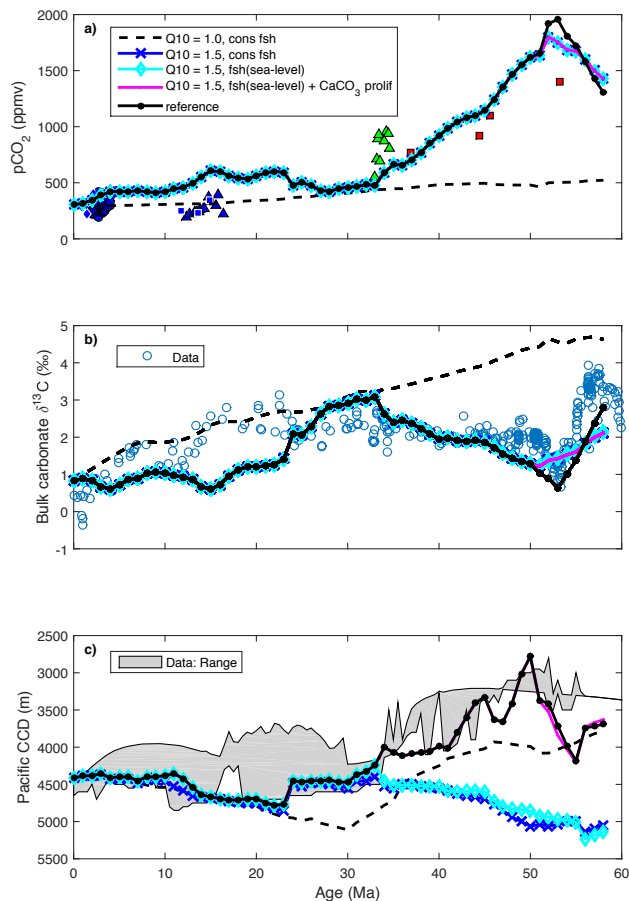
Figure S 18: Selected sensitivity studies results. a) Atmospheric pCO_2. For data legends, refer to Fig. 4. b) Bulk carbonate $\delta^{13}C$ data (open circles) versus different model scenarios. c) Model predicted evolution of the Pacific CCD against the Pacific CCD data range displayed in Fig. 4. The black dashed line corresponds to the control run Figs. 8 and 9. Dark blue line with crosses: temperature dependent Martin curve all other forcings are the same as in the control run. Light blue line with diamonds: same forcings as in the previous run except that shelf-deep $CaCO_3$ fractionation factor (fsh) is a function of sea level change. Magenta: same as the previous run + amplified fsh factor, simulating $CaCO_3$ organism proliferation in the shelf ocean in the Paleocene and Eocene. Black dotted line: same as the previous run, but existence of an organic carbon capacitor assumed during the Late Paleocene Early Eocene.

REFERENCES AND NOTES

1. J. C. Zachos, M. Pagani, L. Sloan, E. Thomas, K. Billups, Trends, rhythms, and aberrations in global climate 65 Ma to present. *Science* **292**, 686–693 (2001).

2. P. K. Bijl, S. Schouten, A. Sluijs, G. J. Reichart, J. C. Zachos, H. Brinkhuis, Early Palaeogene temperature evolution of the southwest Pacific Ocean. *Nature* **461**, 776–779 (2009).

3. B. S. Cramer, J. R. Toggweiler, J. D. Wright, M. E. Katz, K. G. Miller, Ocean overturning since the Late Cretaceous: Inferences from a new benthic foraminiferal isotope compilation. *Paleoceanogaphy* **24**, PA4216 (2009).

4. N. Komar, R. Zeebe, G. Dickens, Understanding long-term carbon cycle trends: The late Paleocene through the early Eocene. *Paleoceanography* **28**, 650–662 (2013).

5. N. Komar, thesis, University of Hawaii, (2017).

6. D. J. Beerling, D. L. Royer, Convergent cenozoic CO_2 history. *Nat. Geosci.* **4**, 418–420 (2011).

7. Y. G. Zhang, M. Pagani, Z. Liu, S. M. Bohaty, R. DeConto, A 40-million-year history of atmospheric CO_2. *Phil. Trans. R. Soc. A* **371**, 20130096 (2013).

8. R. A. Berner, A. C. Lasaga, R. M. Garrels, The carbonate-silicate geochemical cycle and its effect on atmospheric carbon dioxide over the past 100 million years. *Am. J. Sci.* **283**, 641–683 (1983).

9. R. D. Müller, M. Sdrolias, C. Gaina, B. Steinberger, C. Heine, Long-term sea-level fluctuations driven by ocean basin dynamics. *Science* **319**, 1357 (2008).

10. D. G. Van Der Meer, R. E. Zeebe, D. J. van Hinsbergen, A. Sluijs, W. Spakman, T. H. Torsvik, Plate tectonic controls on atmospheric CO_2 levels since the Triassic. *Proc. Natl. Acad. Sci.* **111**, 4380–4385 (2014).

11. A. Ridgwell, R. E. Zeebe, The role of the global carbonate cycle in the regulation and evolution of the Earth System. *Earth Planet. Sci. Lett.* **234**, 299–315 (2005).

12. T. H. van Andel, T. C. Moore, Cenozoic calcium carbonate distribution and calcite compensation depth in the central equatorial Pacific Ocean. *Geology* **2**, 87 (1974).

13. H. Pälike, W. M. Lyle, H. Nishi, I. Raffi, A. Ridgwell, K. Gamage, A. Klaus, G. Acton, L. Anderson, J. Backman, J. Baldauf, C. Beltran, S. M. Bohaty, P. Bown, W. Busch, J. E. T. Channell, C. O. J. Chun, M. Delaney, P. Dewangan, T. D. Jones, K. M. Edgar, H. Evans, P. Fitch, G. L. Foster, N. Gussone, H. Hasegawa, E. C. Hathorne, H. Hayashi, J. O. Herrle, A. Holbourn, S. Hovan, K. Hyeong, K. Iijima, T. Ito, Shin-ichi Kamikuri, K. Kimoto, J. Kuroda, L. Leon-Rodriguez, A. Malinverno, T. C. Moore Jr, B. H. Murphy, D. P. Murphy, H. Nakamura, K. Ogane, C. Ohneiser, C. Richter, R. Robinson, E. J. Rohling, O. Romero, K. Sawada, H. Scher, L. Schneider, A. Sluijs, H. Takata, J. Tian, A. Tsujimoto, B. S. Wade, T. Westerhold, R. Wilkens, T. Williams, P. A. Wilson, Y. Yamamoto, S. Yamamoto, T. Yamazaki, R. E. Zeebe, A Cenozoic record of the equatorial Pacific carbonate compensation depth. *Nature* **488**, 609–614 (2012).

14. B. S. Slotnick, V. Lauretano, J. Backman, G. R. Dickens, A. Sluijs, L. Lourens, Early Paleogene variations in the calcite compensation depth: New constraints using old borehole sediments from across Ninetyeast Ridge, central Indian Ocean. *Clim. Past* **11**, 473–493 (2015).

15. R. E. Zeebe, LOSCAR: Long-term Ocean-atmosphere-Sediment CArbon cycle reservoir model v2.0.4. *Geosci. Model Develop.* **1**, 149–166 (2012).

16. N. Komar, R. Zeebe, Redox-controlled carbon and phosphorus burial: A mechanism for enhanced organic carbon sequestration during the petm. *Earth Planet. Sci. Lett.* **479**, 71–82 (2017).

17. R. A. Berner, Z. Kothavala, GEOCARB III: A revised model of atmospheric CO_2 over Phanerozoic time. *Am. J. Sci.* **304**, 397 (2001).

18. R. W. Eppley, Temperature and phytoplankton growth in the sea. *Fish. Bull.* **70**, 1063 (1972).

19. E. A. Laws, P. G. Falkowski, W. O. Smith, H. Ducklow, J. J. McCarthy, Temperature effects on export production in the open ocean. *Global Biogeochem. Cycles* **14**, 1231–1246 (2000).

20. K. Matsumoto, Biology-mediated temperature control on atmospheric pCO2 and ocean biogeochemistry. *Geophys. Res. Lett.* **34** (2007).

21. L. R. Kump, M. A. Arthur, *Tectonic Uplift and Climate Change* (Springer, 1997), pp. 399–426.

22. L. François, Y. Goddéris, Isotopic constraints on the cenozoic evolution of the carbon cycle. *Chem. Geol.* **145**, 177–212 (1998).

23. K. Wallmann, Controls on the Cretaceous and Cenozoic evolution of seawater composition, atmospheric CO_2 and climate. *Geochim. Cosmochim. Acta* **65**, 3005–3025 (2001).

24. H. Kashiwagi, Y. Ogawa, N. Shikazono, Relationship between weathering, mountain uplift, and climate during the cenozoic as deduced from the global carbon–strontium cycle model. *Palaeogeogr. Palaeoecol.* **270**, 139–149 (2008).

25. R. S. Arvidson, F. T. Mackenzie, M. Guidry, Magic: A Phanerozoic model for the geochemical cycling of major rock-forming components. *Am. J. Sci.* **306**, 135–190 (2006).

26. G. Li, J. Ji, J. Chen, D. B. Kemp, Evolution of the Cenozoic carbon cycle: The roles of tectonics and CO_2 fertilization. *Global Biogeochem. Cycles* **23**, GB1009 (2009).

27. G. Li, H. Elderfield, Evolution of carbon cycle over the past 100 million years. *Geochim. Cosmochim. Acta* **103**, 11–25 (2013).

28. J. K. Caves, A. B. Jost, K. V. Lau, K. Maher, Cenozoic carbon cycle imbalances and a variable weathering feedback. *Earth Planet. Sci. Lett.* **450**, 152–163 (2016).

29. R. van der Ploeg, B. P. Boudreau, J. J. Middelburg, A. Sluijs, Cenozoic carbonate burial along continental margins. *Geology* **47**, 1025–1028 (2019).

30. B. N. Opdyke, B. H. Wilkinson, Surface area control of shallow cratonic to deep marine carbonate accumulation. *Paleoceanography* **3**, 685–703 (1988).

31. S. K. Boss, B. H. Wilkinson, Planktogenic/eustatic control on cratonic/oceanic carbonate accumulation. *J. Geol.* **99**, 497–513 (1991).

32. R. E. Martin, Cyclic and secular variation in microfossil biomineralization: Clues to the biogeochemical evolution of Phanerozoic oceans. *Global Planet. Change* **11**, 1–23 (1995).

33. P. R. Bown, J. A. Lees, J. R. Young, *Coccolithophores* (Springer, 2004), pp. 481–508.

34. P. W. Homewood, The carbonate feedback system; interaction between stratigraphic accomodation, ecological succession and the carbonate factory, *Bull. Soc. Géol. Fr.* **167**, 701–715 (1996).

35. J. Masse, L. Montaggioni, Growth history of shallow-water carbonates: Control of accommodation on ecological and depositional processes. *Inl. J. Earth Sci.* **90**, 452–469 (2001).

36. M. E. Raymo, W. F. Ruddiman, Tectonic forcing of late Cenozoic climate. *Nature* **359**, 117–122 (1992).

37. M. L. Delaney, G. M. Filippelli, An apparent contradiction in the role of phosphorus in Cenozoic chemical mass balances for the world ocean. *Paleoceanography* **9**, 513–527 (1994).

38. J. K. Willenbring, F. von Blanckenburg, Long-term stability of global erosion rates and weathering during late-Cenozoic cooling. *Nature* **465**, 211–214 (2010).

39. S. M. Stanley, Relation of Phanerozoic stable isotope excursions to climate, bacterial metabolism, and major extinctions. *Proc. Natl. Acad. Sci. U.S.A.* **107**, 19185–19189 (2010).

40. C. M. Marsay, R. J. Sanders, S. A. Henson, K. Pabortsava, E. P. Achterberg, R. S. Lampitt, Attenuation of sinking particulate organic carbon flux through the mesopelagic ocean. *Proc. Natl. Acad. Sci. U.S.A.* **112**, 1089–1094 (2015).

41. J. H. Martin, G. A. Knauer, D. M. Karl, W. W. Broenkow, VERTEX: Carbon cycling in the northeast Pacific. *Deep Sea Res.* **34**, 267–285 (1987).

42. K. O. Buesseler, C. H. Lamborg, P. W. Boyd, P. J. Lam, T. W. Trull, R. R. Bidigare, J. K. B. Bishop, K. L. Casciotti, F. Dehairs, Frank, M. Elskens, M. Honda, D. M. Karl, D. A. Siegel, M. W. Silver, D. K. Steinberg, J. Valdes, B. Van Mooy, S. Wilson, Revisiting carbon flux through the ocean's twilight zone. *Science* **316**, 567 (2007).

43. C. J. Bjerrum, J. Bendtsen, J. J. F. Legarth, Modeling organic carbon burial during sea level rise with reference to the Cretaceous. *Geochem. Geophys. Geosyst.* **7**, Q05008 (2006).

44. S. Misra, P. N. Froelich, Lithium isotope history of Cenozoic seawater: Changes in silicate weathering and reverse weathering. *Science* **335**, 818–823 (2012).

45. L. R. Kump, Prolonged Late Permian–Early Triassic hyperthermal: Failure of climate regulation?. *Philos. Trans. R. Soc. A* **376**, 20170078 (2018).

46. J. C. Zachos, G. R. Dickens, R. E. Zeebe, An early Cenozoic perspective on greenhouse warming and carbon-cycle dynamics. *Nature* **451**, 279–283 (2008).

47. Bemis, B. E., H. J. Spero, J. Bijma, D. W. Lea, Reevaluation of the oxygen isotopic composition of planktonic foraminifera: Experimental results and revised paleotemperature equations. *Paleoceanography* **13**, 150–160 (1998).

48. A. K. Hilting, L. R. Kump, T. J. Bralower, Variations in the oceanic vertical carbon isotope gradient and their implications for the Paleoce-Eocene biological pump. *Paleoceanography* **23**, PA3222 (2008).

49. A. Kurtz, L. R. Kump, M. A. Arthur, J. C. Zachos, A. Paytan, Early Cenozoic decoupling of the global carbon and sulfur cycles. *Paleoceanogr. Paleoclimatol.* **18**, 1090 (2003).

50. E. Anagnostou, E. H. John, K. M. Edgar, G. L. Foster, A. Ridgwell, G. N. Inglis, R. D. Pancost, D. J. Lunt, P. N. Pearson, Changing atmospheric CO_2 concentration was the primary driver of early Cenozoic climate. *Nature* **533**, 380 (2016).

51. P. N. Pearson, G. L. Foster, B. S. Wade, Atmospheric carbon dioxide through the eocene-oligocene climate transition. *Nature* **461**, 1110–1113 (2009).

52. G. L. Foster, C. H. Lear, J. W. Rae, The evolution of pCO_2, ice volume and climate during the middle Miocene. *Earth Planet. Sci. Lett.* **341**, 243 (2012).

53. G. Bartoli, B. Hönisch, R. E. Zeebe, Atmospheric CO2 decline during the Pliocene intensification of northern hemisphere glaciations. *Paleoceanography* **26**, PA4213 (2011).

54. O. Seki, G. L. Foster, D. N. Schmidt, A. Mackensen, K. Kawamura, R. D. Pancost, Alkenone and boron-based pliocene pCO$_2$ records. *Earth Planet. Sci. Lett.* **292**, 201–211 (2010).

55. S. M. Campbell, R. Moucha, L. A. Derry, M. E. Raymo, Effects of dynamic topography on the cenozoic carbonate compensation depth. *Geochem. Geophys. Geosyst.* **19**, 1025 (2018).

56. T. H. van Andel, Mesozoic/Cenozoic calcite compensation depth and the global distribution of calcareous sediments. *Earth Planet. Sci. Lett.* **26**, 187–194 (1975).

57. D. L. Royer, Y. Donnadieu, J. Park, J. Kowalczyk, Y. Goddéris, Error analysis of CO$_2$ and O$_2$ estimates from the long-term geochemical model GEOCARBSULF. *Am. J. Sci.* **314**, 1259–1283 (2014).

58. R. E. Zeebe, D. A. Wolf-Gladrow, *CO$_2$ in Seawater: Equilibrium*, *Kinetics*, *Isotopes* (Elsevier Oceanography Series, 2001), pp. 346.

59. J. Veizer, D. Ala, K. Azmy, O. Bruckschen, D. Buhl, F. Bruhn, G. A. F. Carden, A. Diener, S. Ebneth, Y. Goddéris, T. Jasper, C. Korte, C. F. Pawellek, O. G. Podlaha, H. Strauss, ^{87}Sr/^{86}Sr, δ^{13}C and δ^{18}O evolution of Phanerozoic seawater. *Chem. Geol.* **161**, 59–88 (1999).

60. T. Westerhold, U. Rohl, B. Donner, H. K. McCarren, J. C. Zachos, A complete high-resolution Paleocene benthic stable isotope record for the central Pacific (ODP Site 1209). *Paleoceanography* **26**, PA2216 (2011).

61. G. R. Dickens, J. Backman, Core alignment and composite depth scale for the lower Paleogene through uppermost Cretaceous interval at Deep Sea Drilling Project Site 577. *Newslett. Stratigraphy* **46**, 47–68 (2013).

62. R. Samworth, H. Poore, Understanding past ocean circulations: A nonparametric regression case study. *Stat. Model.* **5**, 289 (2005).

63. H. Poore, R. Samworth, N. White, S. Jones, I. McCave, Neogene overflow of northern component water at the greenland-scotland ridge. *Geochem. Geophys. Geosyst.* **7**, Q06010 (2006).

64. T. Tyrrell, The relative influences of nitrogen and phosphorus on oceanic primary production. *Nature* **400**, 525–531 (1999).

65. J. L. Sarmiento, N. Gruber, *Ocean Biogeochemical Dynamics: Princeton* (Princeton Univ. Press, 2006).

66. P. Van Cappellen, E. D. Ingall, Redox stabilization of the atmosphere and oceans by phosphorus-limited marine productivity. *Science* **271**, 493 (1996).

67. L. R. Kump, S. L. Brantley, M. A. Arthur, Chemical weathering, atmospheric CO$_2$, and climate. *Annu. Rev. Earth Planet. Sci.* **28**, 611–667 (2000).

68. S. Flögel, K. Wallmann, C. J. Poulsen, J. Zhou, A. Oschlies, S. Voigt, W. Kuhnt, Simulating the biogeochemical effects of volcanic CO$_2$ degassing on the oxygen-state of the deep ocean during the cenomanian/turonian anoxic event (OAE2), *Earth Planet. Sci. Lett.* **305**, 371–384 (2011).

69. T. Tyrrell, R. E. Zeebe, History of carbonate ion concentration over the last 100 million years. *Geochim. Cosmochim. Acta* **68**, 3521 (2004).

70. H. W. Menard, S. M. Smith, Hypsometry of ocean basin provinces. *J. Geophys. Res.* **71**, 4305 (1966).

71. K. L. Bice, E. J. Barron, W. H. Peterson, *Tectonic Boundary Conditions for Climate Reconstructions*, T. J. Crowley, K. C. Burke, Eds. (Oxford Univ. Press, 1998), pp. 227–247.

72. N. Herold, M. Seton, R. D. Müller, Y. You, M. Huber, Middle Miocene tectonic boundary conditions for use in climate models. *Geochem. Geophys. Geosyst.* **9**, Q10009 (2008).

73. M. F. Stuecker, thesis, Carl-von-Ossietzky Universität Oldenburg, Germany (2009).

74. M. F. Stuecker, R. E. Zeebe, Ocean chemistry and atmospheric CO2 sensitivity to carbon perturbations throughout the cenozoic. *Geophys. Res. Lett.* **37**, L03609 (2010).

75. J. R. Toggweiler, Variation of atmospheric CO_2 by ventilation of the ocean's deepest water, *Paleoceanography* **14**, 571–588 (1999).

76. C. Slomp, P. Van Cappellen, The global marine phosphorus cycle: Sensitivity to oceanic circulation. *Biogeosciences* **4**, 155–171 (2007).

77. I. Tsandev, C. Slomp, Modeling phosphorus cycling and carbon burial during cretaceous oceanic anoxic events. *Earth Planet. Sci. Lett.* **286**, 71–79 (2009).

78. K. Wallmann, Feedbacks between oceanic redox states and marine productivity: A model perspective focused on benthic phosphorus cycling. *Global Biogeochem. Cycles* **17**, 1084 (2003).

79. R. A. Berner, GEOCARB II: A revised model of atmospheric CO_2 over Phanerozoic time. *Am. J. Sci.* **294**, 56–91 (1994).

80. M. Iversen, H. Ploug, Temperature effects on carbon-specific respiration rate and sinking velocity of diatom aggregates–potential implications for deep ocean export processes. *Biogeosciences* **10**, 4073–4085 (2013).

81. T. K. Lowenstein, R. V. Demicco, Elevated eocene atmospheric CO_2 and its subsequent decline. *Science* **313**, 1928 (2006).

82. M. A. Kominz, J. V. Browning, K. G. Miller, P. J. Sugarman, S. Mizintseva, C. R. Scotese, Late Cretaceous to Miocene sea-level estimates from the New Jersey and Delaware coastal plain coreholes: An error analysis. *Basin Res.* **20**, 211–226 (2008).

83. M. Raitzsch, B. Hönisch, Cenozoic boron isotope variations in benthic foraminifers. *Geology* **41**, 591–594 (2013).